JOINT EUROPEAN TORUS

JET–P(87)44

A. Boileau, M. Von Hellermann, L.D. Horton, J. Spence
and H.P. Summers

The Deduction of Low-Z Ion Temperature and Densities in the JET Tokamak using Charge Exchange Recombination Spectroscopy

The Deduction of Low-Z Ion Temperature and Densities in the JET Tokamak using Charge Exchange Recombination Spectroscopy

A. Boileau, M. Von Hellermann, L.D. Horton, J. Spence and H.P. Summers

JET-Joint Undertaking, Culham Science Centre, OX14 3DB, Abingdon, UK

Preprint of Paper to be submitted for publication in
Plasma Physics and Controlled Fusion

ABSTRACT

Charge exchange recombination spectroscopy (CXRS) has been used on JET to study fully stripped low-Z species. The ion temperature in the plasma centre was measured from visible lines of helium, carbon and oxygen excited by charge exchange with heating neutral beam particles. A cold component produced at the plasma edge was apparent on helium and carbon spectra. The charge exchange feature was unambiguously isolated for the various composite lines and all three impurities agreed on the same temperature within the experimental error. Toroidal rotation velocity measurements near r/a ~0.65 on the high field side are also presented. Observed column emissivities were converted into absolute impurity densities using a neutral beam attenuation code and charge exchange effective rate coefficients. Comprehensive new calculations were performed to obtain the effective rate coefficients. The models took detailed account of cascading and the influence of the plasma environment in causing ℓ-mixing, and allowed the n-dependence of the rate coefficients to be addressed experimentally using some carbon transitions. The effective ion charge reconstructed from simultaneous measurements of the densities of dominant impurities shows good agreement with the value inferred from visible bremsstrahlung. Helium (helium discharge or minority RF heating), carbon and oxygen concentrations were monitored during characteristic operating regimes. Significant differences in the ratio of these impurities were observed.

1. INTRODUCTION

In modern fusion experiments such as JET, the fully stripped species H^+, D^+, He^{+2}, C^{+6} and O^{+8} represent the bulk of the hot plasma core. The controlled fusion goal requires comprehensive understanding of the dynamics and kinematics of these particles. The bremsstrahlung radiation emitted by stripped ions in ohmically heated plasmas only allows spectroscopic measurement of Z_{eff} averaged over a line of sight. It does not provide resolvable features for individual species. Emission spectroscopy usually concentrates on low level transitions of ions excited by electron impact. In JET, the associated emission shells for light impurities occur in the plasma periphery. Central abundances must then be inferred via an impurity transport model based on the peripheral measurements. This situation has been revolutionised by the introduction of neutral beam heating.

Useful diagnostic spectroscopic line measurements are possible on impurity elements which are fully ionised in the central region of plasmas penetrated by neutral hydrogen beams. This is because of the efficient charge exchange reaction

$$A^{+Z} + H \rightarrow A^{+Z-1}(n\ell j) + H^+ \qquad (1)$$

where Z is the nuclear charge, H denotes any isotope of hydrogen and $n\ell j$ are the recombined hydrogen-like ion quantum numbers. It follows from the fact that principal quantum shells n populated by this reaction tend to be highly excited that the cascade radiation emitted after capture can be observed in the visible. Wavelength calibrated measurements of spectral profiles can be interpreted in terms of impurity ion temperature and plasma rotation velocity, and intensity calibrated measurements of photon fluxes in terms of local impurity densities.

Progress in 'charge exchange recombination spectroscopy' (CXRS) has been rapid. Measurements of local ion temperature have been performed using CXRS on many tokamak experiments[1-6]. This diagnostic has also been used to investigate toroidal plasma rotation [2,7-9]. Radial profiles of these spatially resolved measurements have been obtained either on a shot-to-shot basis[9] or by using a multichord system[10,11]. Less common are calculations of absolute ion densities using measured CXRS line intensities [12-18]. Recent work at PBX[19] has used relative impurity density profiles for comparison with convective transport models. These results have demonstrated clearly the diagnostic potential of CXRS and have pointed to the need for detailed analysis and quantitative interpretation of absolutely calibrated photon fluxes. The justification for the present paper is in the steps taken towards this quantitative assessment and in the description of the exploitation of the diagnostic on JET.

The CXRS diagnostic makes use of the heating beams as a source of high energy neutrals. An essential feature is the concentration on the visible part of the spectrum. Fibre optics transfer the radiation to remote instruments separated by biological shields from the experiment. The immediate aim has been the investigation of specific spectral features of visible charge exchange lines of low Z impurities. When measurements are restricted to visible wavelengths, the interpretation, especially in terms of impurity densities, depends quite sensitively on beam particle energies and states and on the plasma environment of the radiating ions. The description of these effects relies heavily on theoretical atomic data and the emission models become quite complex. It will be shown that these models are justified in that the trends of variation of observed results with plasma conditions are more closely reproduced. On the other hand, at a refined quantitative level, it is evident that the analysis provides a comment on the theoretical data as well as an interpretation of the plasma. The breadth of experimental data available to us from JET has encouraged us to suggest preliminary corrections to some of the theoretical data.

While the initial impact of this work at JET is in the study of the light species, helium (added during minority RF heating or wall conditioning discharges), carbon and oxygen, charge exchange recombination may provide fruitful diagnostics near ignition for fusion product alpha particles. The density of other impurities such as beryllium, a future limiter material, may also become sufficiently large to allow measurements of charge exchange recombination lines. Finally, VUV and X-ray spectral line measurements associated with charge exchange recombination, just becoming possible on JET, will supplement the visible measurements and allow more comprehensive comment on theoretical models. For these reasons, we provide in the paper a model for charge exchange line emission analysis of greater generality than the immediate need in JET.

Turning to the order of the paper, Section 2 begins with an overview of the JET environment as it pertains to charge exchange recombination and its interpretation. Then the actual experimental set-up for CXRS, its geometry and capability on JET are described. Also the important related details of neutral heating beam shape, particle distribution and attenuation are given.

Section 3 is concerned with line shapes. Since the paper is devoted mostly to spectral lines emitted in transitions between whole principal quantum levels of hydrogenic ions, the observed lines are expected to be overlayed composites of fine structure components, Doppler broadened by ion thermal motion and Doppler shifted by toroidal rotational motion of the bulk plasma. The column emissivity associated with CXRS along an observational line of sight would take the form

$$\frac{dI}{d\lambda}(n\rightarrow n') = \sum_{\ell j,\ \ell' j'} A(n\ell j\rightarrow n'\ell' j') \int N(A^{+z-1}_{n\ell j})\ \phi_\lambda(m,v,T_Z)dx \qquad (2)$$

where N denotes the impurity number density, A(i→j) is the Einstein coefficient and ϕ represents the component spectral profile, with T_Z the impurity ion temperature, m the ion mass and v the bulk plasma rotational speed projected on the line of sight. In fact the main broad CXRS feature from the beam interaction in the hot plasma core is usually distorted by overlapping narrower features formed at the edge of the plasma. It will be shown that the charge exchange feature can be isolated from the composite line profile, allowing values of v and T_Z to be deduced.

The column emissivity of the broad CX feature in a line n→n' (integrated over wavelength) resulting from charge exchange in the presence of a neutral beam can alternatively be written as

$$I(n\to n') = q^{CEM}_{(n\to n')} \int N(H)N(A^{+z})d\ell \qquad (3)$$

where $q^{CEM}_{(n\to n')}$ is an 'effective charge exchange recombination coefficient' leading to emission of the line $n\to n'$, and $\int N(H)N(A^{+z})d\ell$ is the 'charge exchange emission measure'. For a localised intersection of neutral beams, plasma and spectroscopic line of sight, this is a useful separation. In Section 4, the theory is developed for calculating $q^{CEM}_{(n\to n')}$ for arbitrary ions and transitions and for refinement of $q^{CEM}_{(n\to n')}$ based on observations. This theory will also provide details on $N(A^{+z-1}_{n\ell j})$ required in equation (2). The emission measure is itself a useful quantity for interpretation of relative impurity concentrations. However, knowledge of beam geometry, viewing geometry and attenuation allows separation from the emission measure of the component density $N(A^{+z})$. The additional theoretical analysis of beam attenuation required is developed in Section 4.5. In Section 4.6, the emission measure theory is extended in two ways. Firstly, alternate primary excitation processes besides charge exchange from hydrogen beams are allowed. The new processes include electron impact excitation from the ground state and charge exchange recombination from thermal hydrogen in an excited level. Secondly, lithium and sodium-like recombined systems are considered. This extended theory is sufficient to allow quantitative investigation of the features formed at the cold plasma edge and superimposed onto the CX signal for some of the transitions observed. It is also used to provide some broad predictions of series variation of effective coefficients for quantitative XUV and UV observations of charge exchange.

In Section 5, some analysis is given of central impurity densities in JET. This establishes characteristic behaviour of light impurities in JET in the presence of neutral hydrogen beam heating under various modes of operation. In Section 5.2, possible adjustments of the theory are investigated in the light of the JET analysis. Section 5.3 provides a preliminary examination of the cold feature observed on carbon spectra. The conclusions are in Section 6.

2. THE JET CHARGE EXCHANGE RECOMBINATION DIAGNOSTIC

2.1 Species and the plasma environment

The dominant light impurities in JET are carbon and oxygen[20]. These are both suitable for diagnostic charge exchange measurements as is helium, introduced as a minority constituent during RF heating. Beryllium and the medium Z elements neon and argon added for specific diagnostic and calibration studies may also be suitable. The hydrogen-like stages of these elements emit convenient visible line radiation in the central regions of the plasma following charge exchange recombination with neutral hydrogen heating beams. Visible $\Delta n=1$ and $\Delta n=2$ spectrum lines of these species are listed in Table I. The wavelength is the intensity weighted average of the various angular components in air. The width of the whole collection of supermultiplets in the $n \rightarrow n'$ transitions is also given. It is to be noted that a number of blending coincidences occur both between impurity lines and with hydrogen. Table I also gives the emission measure for capture from H(1s) for each line axis, based on a standard set of JET plasma conditions, required to produce a column emissivity of 1×10^{12} ph/cm^2/sec for a beam energy of 50 keV/amu. This is an approximate indication of detectability.

A similar class of features can be emitted by lithium-like and sodium-like ions following charge exchange capture by the corresponding helium-like or neon-like ions from neutral hydrogen beams. In smaller tokamaks, medium Z species such as Ar in its helium-like stage, and heavier species such as K in its neon-like stage have been used in charge exchange studies[18]. (For JET light and medium Z species are fully stripped in central plasma.) For completeness therefore some data on lithium-like and sodium-like ions is given in tables II and III respectively. In these cases, the spread in wavelength of the components of the complete n→n' shell lines is very large. Practical spectroscopic measurements are likely to encompass an incomplete set of components. The values given in tables II and III give only a broad indication of expected emission.

Lithium-like line emission from high levels of light species does occur in JET, but is an edge plasma feature and its origin is not charge exchange from beam hydrogen. This point is considered later in the discussion of cool components.

The influence of the plasma environment in JET and the charge exchange reaction on the principal emitting ions is summarised approximately in Table IV. For typical plasma central temperature and various densities, a series of special n values indicate the influential atomic processes in charge exchange recombination line formation. n_{crit} is the principal quantum number at which the charge exchange capture cross-section maximises. Evidently most of the visible lines are emitted in transitions from levels above n_{crit} where the cross-sections for charge exchange are decaying with n. n_{ion} is the principal quantum number marking the thermal collision limit defined here as the level n at which

$$\frac{N_e\, q^{ion}(n)}{A(n,n-1 \rightarrow n-1,n-2} = 1 \qquad (4)$$

n_{mix} is the level at which ℓ mixing by particle collisions becomes significant defined here as the level n for which

$$\frac{N_I q_I(n,n-1 \rightarrow n,n-2)}{A(n,n-1 \rightarrow n-1,n-2)} = 1 \qquad (5)$$

We have assumed for this purpose that $Z_{eff} = 2$. N_I is the number density of Z_{eff} ions so that $N_I = \frac{1}{2} N_e$. $q^{ion}(n)$ is the electron impact ionisation rate coefficient from principal quantum level n, $A(n\ell \rightarrow n'\ell')$ the $n\ell$ shell resolved coefficient and $q_I(n\ell \rightarrow n\ell')$ the ion impact induced transition rate coefficient. The electron temperature given in the table is used in these estimates. In Section 4, the influence of these parameters on the structure of our atomic models for line emission will be examined in detail.

2.2 Experimental configuration

2.2.1 The JET heating neutral beams

The CXRS diagnostic uses the heating neutral beams on JET as probe beams. These are shown in Fig.1, together with the CXRS lines of sight. The neutral beam sources were operated at acceleration voltages up to 80 keV, with a maximum injected power of 10 MW. The total neutral power injected into the plasma is split into full, half and third energy components, with a species mixture of 76:17:7 for deuterium injection[21].

In order to compute local impurity ion densities from measured CX column emissivities the fast neutral particle density along the observation line of sight has to be calculated. Detailed calorimetric investigations in the JET neutral beam test bed facilities have shown that the neutral beam profile inside the plasma - that is, far from the ion source - can be approximated by a Gaussian beam profile, diverging from a single point source[22]. A detailed description of the local neutral particle density calculation is given in Section 4.5.

2.2.2 Layout of the CXRS diagnostic viewing lines

The layout of the two active CXRS lines of sight intersecting the neutral beams and the single passive line of sight used for the measurement of background spectra is shown in Fig.1. The vertical active CXRS line of sight intersects all eight beams, with a contribution to the neutrals density from the normal beams larger than from the tangential beams (Fig.2). The intersection volume is located at a major radius $R=(3.03\pm0.05)$m and allows a central measurement of low-Z impurity ion temperature and density. The vertical extent of the active volume depends on the number of beam sources fired during a JET pulse and has a maximum of approximately ± 30 cm if all eight sources are contributing to the CXRS signal. It remains in any case much smaller than the gradient scale length of the density and temperature profiles in the central region so that the measurements are representative of plasma parameters on axis.

The horizontal line of sight intersects the two lower neutral beams at a major radius of 2.3 m ($r/a=0.65$). Light collected along this line of sight is analysed to give another localised point in the impurity ion temperature profile as well as the bulk plasma toroidal rotation at that major radius.

The passive line of sight is identical to the active vertical viewing line in the adjacent octant but does not intersect any of the neutral beams. It is used for simultaneous measurement of background spectra. This is discussed further in Section 3.

2.2.3 Optical links and spectroscopic apparatus

The optical heads of the viewing lines consist of short focal length quartz lenses (f=32 mm, F/1.6) which image the active volume onto 1 mm quartz fibre. The radiation resistant fibres of 120 m length transfer the collected light to a remote diagnostic hall separated by a biological shield from the torus hall[23]. The fibre link and the absence of instrumentation near the torus is an essential feature for continued operation of this diagnostic in the active phase of JET. The transmitted light which covers the visible spectrum between 4000 Å and 7000 Å is analysed by two spectrometers. The optical arrangement is shown in Fig.3.

Carbon is the dominant low-Z impurity in JET plasmas with typical densities of a few percent of the electron density. For this reason its strongest transition in the visible (8 to 7 at 5290.5Å) was used as a routine CXR diagnostic line. As shown in Fig.3, one spectrometer is dedicated solely to analysis of this transition, while the second can monitor any of the other CX lines. This is achieved by passing the light through a 45° tilted band pass filter, transmitting the 5290.5Å spectrum and reflecting the remaining visible light into the second spectrometer. This setup thus allowed transitions from two impurities emitting from the same active volume to be monitored simultaneously.

Using the arrangement shown in Fig.3 and the dual entrance feature of SPEX 1269 Czerny Turner spectrometers, it was also possible to record the light emitted at two different radii (R~3.03 m and R~2.3 m) or to monitor the signal collected with the active and passive vertical lines of sight.

The spectra were recorded by linear intensified detector arrays (EG&G 1420). The controlling system includes a 16 bit digitizer and reads a prespecified detector pixel range to the host computer. Spectral profiles covering normally 300 to 600 pixels were recorded for 20 to 80 time slices during a JET pulse, the exposure time varying according to the strength of the CX transition being monitored. For the 5290.5Å carbon transition, exposure times as low as 10 msec with a repetition rate of 50 Hz are possible allowing resolution of sawteeth oscillations on the central impurity ion temperature.

The complete system including optical head, fibre, imaging optics, spectrometer and detector was absolutely calibrated by a procedure routinely used on JET for the visible bremsstrahlung measurements[23]. Since in-torus calibration is not possible on JET during operational periods, window transmission losses were calculated from manufacturer's specifications rather than directly measured. Representative calibration factors given by the ratio of incident photon fluxes and recorded count rates are in the order of 1.0×10^6 photons/cm**2/sr/count at a wavelength of 5290.5 Å using a

200 μ slit and the SPEX 1702 spectrometer. Routine checks have shown that absolute calibrations are reproducible within 10%.

The spectrometers were used normally at a fixed entrance slit of 200 μ corresponding to a wavelength width of 1.0Å at 5290.5Å. The instrument function at this slit width can be approximated by a sum of several Gaussians (two are usually sufficient). This approximation considerably simplifies the deconvolution of instrument profiles and spectral Doppler-broadened profiles (cf. Section 3.1). For JET plasmas with central impurity ion temperatures ranging between 3 keV for purely ohmic heated plasmas and 12 keV for low density, high temperature, neutral beam heated plasmas, Doppler widths for the different lines observed range from 3Å to 16Å.

3. ION TEMPERATURE AND TOROIDAL PLASMA ROTATION VELOCITY

Charge exchange recombination spectroscopy measurements of visible spectrum lines of the intrinsic primary impurities have been made on JET. These have provided the impurity ion temperature and toroidal plasma rotation velocity for neutral beam heated plasmas. Also, they have provided data on the possible variation of ion temperature with ion mass. The measured impurity lines are He II 4685.2 Å; C VI 5290.5 Å, 4498.8 Å and O VIII 4340.5 Å, 6083.3 Å. In addition, the charge exhange feature of H I 6562.8 Å has been measured. It has been a matter of concern to extract from each measurement, an unambiguous signal indicative of only the impurity ion Doppler motion in the active region. For this reason, we discuss the individual line measurements and analysis in detail in Section 3.1. It will be seen that the dual spectrometer arrangement described in Section 2.2.3 has been of significance in establishing confidence in the analysis. In Section 3.2 deductions from the measurements about the JET plasma behaviour are reviewed.

3.1 Experimental analysis of Doppler broadened spectra on JET

Typical measured spectrum line profiles are shown in the following figures

O VIII	n= 9-8	4340.5 Å	Fig.4
O VIII	n=10-9	6068.3 Å	Fig.5
C VI	n= 8-7	5290.5 Å	Fig.6
C VI	n=10-8	4498.8 Å	Fig.7
He II	n= 4-3	4685.2 Å	Fig.8
H I	n= 3-2	6562.8 Å	Fig.9

It is evident that in general the profiles are composite. The dominant broad feature arises from charge exchange in the active volume. The narrow lines originate from the plasma edge and are not directly excited by the neutral beams. It is our contention that the Gaussian profile of the broad feature can be extracted uniquely from the measured composite profile and that it correctly describes the ion temperature in the active volume. The procedure is as follows:

The measured spectra are first converted to absolute fluxes. This is performed using a fit to the detector calibration as a function of pixel number. Not only does the detector response vary across the 700 intensified pixels but the beam splitter also introduces wavelength dependencies which can be significant for certain transitions. This pre-regression calibration is particularly important for hydrogen and helium temperature determinations where the spectra cover most of the detector. A standard nonlinear fitting code is then used to represent the profile with a multiple Gaussian and to provide an estimate of the statistical errors (normally <10%). A background level, due to bremsstrahlung, is also extracted. In certain cases the fitting is constrained by specifying a known transition wavelength.

The O VIII 4340.5 Å line (Fig.4) appears on the long wavelength wing of the D_γ line. An estimate of the O VIII line wavelength as a theoretical column emissivity weighted average of the ℓ-resolved contributing multiplets is within 0.05 Å of the measured value. In the light of this agreement, and for weak charge exchange signal analysis, the wavelength of this line is usually fixed with respect to the neighbouring D_γ line. The spectrum can then be truncated to exclude interfering O II lines arising from inflowing oxygen ions from the walls.

The O VIII 6068.3 A line (Fig.5) appears essentially as a single Gaussian at the expected wavelength. It should however we pointed out that due to the low effective excitation rate $(q^{CEM}(10\rightarrow9) \simeq 0.4\ q^{CEM}(9\rightarrow8))$ and due to low oxygen levels ($\lesssim$ 1%), the poor signal strength does not allow a clear separation of additional narrow features which are sometimes observed. For this reason, the 10→9 line does not seem to be a suitable candidate for measuring the impurity ion temperature. The total charge exchange column emissivity is however little affected by those additional lines and the spectrum can be used to deduce the oxygen concentration.

The C VI 5290.5 A line (Fig.6) is well represented by two Gaussians at the expected wavelength and a further Gaussian representing an O IV peripheral ion line near 5305.5 A. The cold component appearing at the same wavelength as the charge exchange signal is discussed in Section 5.4. We note that the feature is present before and during neutral beam injection. Simultaneous observation of the cold component by the passive line of sight (see Section 2.3), which does not intersect the neutral beams and so has no hot charge exchange signal, shows the same temperature behaviour as the cold feature in the active viewing line (Fig.10). The C VI 4498.8 A line (Fig.7) is weaker but in other respects is similar to the other carbon transition. The temperature of the cold carbon component ranges typically from 200 eV to 600 eV but can rise to 1.0-1.5 keV in low density, high temperature discharges. Simultaneous measurements of the C VI 5290.5 A and C VI 4498.8 A transitions along the same line of sight made using the dual spectrometer arrangement are described in Section 5.3.

For He II 4685.2 A (Fig.8), a three Gaussian fit must be used, one for the hot charge exchange component and the other two representing cold components. In the ohmic regime on JET, two Gaussians are clearly necessary to fit the narrow helium 4685.2 A line[24]. Their temperatures range from 50 eV to 100 ev, and from 300 eV to 700 eV.

The deuterium Balmer Alpha spectrum (Fig.9) has a very complex structure consisting of an extremely broad charge exchange feature and several additional narrow components. The complexity of the spectrum makes direct access to central deuterium temperature and density difficult. The broad charge exchange component is, in general, a composite hydrogen/deuterium profile. This will lead to two broad features of different width and amplitude. For some JET operating conditions the hydrogen concentration is low enough so that the hydrogen CX feature can be neglected.

A more serious constraint is Balmer Alpha radiation emitted by beam particles, which have been excited by collisions with plasma electrons. This light is Doppler shifted by the beam velocity and its spectral width is determined by the beam divergence (assuming as monochromatic beam acceleration voltage). For our vertical line of sight which intersects four pairs of neutral beams at slightly different angles the result is a group of up to 12 overlapping lines which cannot be clearly separated from the charge exchange signal.

It should however be emphasized that the Balmer Alpha spectrum has special diagnostic potential for non-perpendicular lines of sight where beam particle emission features are Doppler shifted into the far wings of the CX profile. It will not only provide direct access to central bulk plasma ion temperatures but will also enable the investigation of energy deposition and central dilution factors during injection. In principle the beam components measured at several radii will give direct information on beam attenuation.

To summarise, it has been shown that the hot charge exchange feature originating from the active volume can be isolated for the various impurity lines. Our preferred line for systematic temperature analysis on JET is C VI 5290.5 Å.

Only the most intense lines, namely C VI 5290.5 Å and O VIII 4340.5 Å can be used for rotation velocity measurements near R~2.3 m (see Fig.1), since the neutral beams are strongly attenuated at that radius. Fig.11a shows a profile for the C VI 5290.5 Å transition with a displaced hot component. The reference position for velocity calculation is determined from the cold component position before injection, assuming that the rotation velocity of C VI ions near the edge is negligible during the Ohmic phase. For the O VIII 4340.5 Å line (Fig.11b), the narrower D_γ line is used as a reference. Toroidal velocity measurements using this transition can only be made because the parasitic O II emission lines observed with the vertical line of sight looking at the top of the vessel are clearly negligible for measurements with the horizontal line of sight looking at the bottom of a limiter during

X-point operation. The spectral interval can therefore be expanded towards the longer wavelengths to which the CX signal is shifted.

3.2 Characteristic Results on JET

3.2.1 Rotation velocity

Plasma rotation velocity near R~2.3 m was measured with a time resolution of 100-250 msec limited by weak charge exchange signal strengths due to attenuated neutral beams. Sample results for the C VI 5290.5 Å and O VIII 4340.5 Å transitions are given in Fig.12. These show that the rotation velocity maximises after a few hundred msec at fixed beam power and increases with neutral beam power. Scaling of rotation velocity at R~2.3 m (r/a~0.65) with $P_{NB}/\langle N_e\rangle_\ell$ using the few available experimental points corresponding to quasi equilibrium conditions remains inconclusive. It is clear however that smaller values of rotation velocity are associated with lower ion temperatures (at R~2.3 m) as shown in Fig.13. This figure includes transient values. It is unlikely that this result is an artifact of the diagnostic since a similar result is obtained if the electron temperature from the same magnetic surface is used instead of the charge exchange impurity ion temperature. Also, measurements made with the two charge exchange lines used for toroidal rotation velocity calculation appear to follow the same trend.

3.2.2 Low Z impurity ion temperatures

It is firstly evident that there is close agreement between helium, carbon and oxygen temperatures in JET as inferred from charge exchange lines (Fig.14). On the basis of these results, any mass dependence on the light impurity temperatures must be less than 5-10% (the experimental error bars on the temperatures).

Depending upon the operating conditions of JET during additional heating, the impurity ion temperature can be much larger (Fig.15a) or just comparable (Fig.15b) to the electron temperature. In both cases the charge exchange impurity ion temperature follows the sawtooth relaxations. The scaling of the impurity temperature in the plasma centre with neutral beam power (normalised to the electron density on axis) is shown in Fig.16. The data were averaged over sawteeth periods to reduce the data scatter $((\Delta T_Z)_{saw} \lesssim 3$ keV). It illustrates the merit of the H-mode regime during X-point operation where a slightly higher ion temperature is achieved with only half the additional heating per particle required in the L-mode regime.

4. THEORY OF IMPURITY DENSITY DETERMINATION FROM OBSERVED LINES

Reduction of observed column emissivities to local impurity number densities is usefully viewed as two steps. Firstly, the data is reduced to an 'emission measure', a step depending on a theoretical model of atomic reactions involving the emitting species. Then local densities are inferred from the emission measure, this step depending on a detailed model for neutral hydrogen beam attenuation. An advantage of this approach is that knowledge of emission measures allows comparison of densities of different species and comment on the theoretical models without full information on beam attenuation. In the following, reference is made to $n\ell$ levels without loss of generality in application to an $n\ell j$-resolved picture.

4.1 Emission measure

The reaction

$$A^{+z} + H(1s) \rightarrow A^{+z-1}(n\ell) + H+ \qquad (6)$$

is the primary direct reaction populating excited levels $n\ell$ of hydrogen-like ions of nuclear charge z in the centre of JET, in the presence of neutral H(1s) beams. If this is the sole recombination mechanism active, then (c.f. Section 1) for an observed column emissivity $I(n\rightarrow n')$, it prompts a separation into a 'charge exchange emission measure' (CEM) given by

$$\int N(H(1s))\, N(A^{+z})d\ell \qquad (7)$$

and an effective rate coefficient for the specific line emission $q^{CEM}_{H(1s)}(n \rightarrow n')$. The distinction is stressed between effective rates which are the composite result of capture onto various levels, level population mixing and cascade, and the individual primary capture rates onto specific levels. For nearly homogeneous plasma conditions in the interaction region, the separation is meaningful and $q^{CEM}_{H(1s)}(n \rightarrow n')$ has negligible dependence on $N[H(1s)]$ and $N(A^{+z})$. q is determined theoretically from a population balance model. If this model were perfect, one observed line would be sufficient to obtain the exact emission measure. Routine analysis on JET is based on this assumption. One spectrum line is observed for each species and this is reduced to a local density using stored tabulations of $q^{CEM}(n \rightarrow n')$ and a simultaneous attenuation calculation. In directed investigations however, several spectrum lines may be observable from the same ion either simultaneously or under the same emission conditions. This allows determination of a best estimate of the emission measure and a differential comparison of experimental and theoretical reaction rates. The direct capture rate coefficients are in general the most difficult to calculate theoretically and so subject to the greatest uncertainty. The approach here is to seek comparison between experimental and theoretical estimates of the primary direct rates. The broad principle is as follows: suppose m spectrum lines are observed simultaneously from the same ion with different upper levels of the emitting transition

$$n_1, \ldots, n_m$$

then the measurement reduction is organised to give the emission measure and the ratios $\frac{q_{n_1}^{exp}}{q_{n_1}^{theor}}, \ldots, \frac{q_{n_m}^{exp}}{q_{n_m}^{theor}}$ subject to

$$q_{n_1}^{exp} + \ldots + q_{n_m}^{exp} = q_{n_1}^{theor} + \ldots + q_{n_m}^{theor} \qquad (8)$$

The matrix manipulations are quite elaborate and details are given in appendix A. The theoretical calculations used for direct charge exchange capture coefficients will be discussed in Section 4.3.

4.2 Population and level mixing models

The calculation of excited level populations of impurity ions in plasma has been discussed in some detail by Spence & Summers[25]. The present paper follows the same approach although a rather more restricted view is adopted orientated to observed line interpretation. Subsequent to the primary direct capture process, it is supposed that four further reaction processes redistribute the excited level populations. These are

spontaneous emission

$$A^{+z-1}(n\ell j) \rightarrow A^{+z-1}(n'\ell'j') + h\nu, \qquad (9)$$

collisional ionisation by electrons

$$A^{+z-1}(n\ell j) + e \rightarrow A^{+z} + e + e, \qquad (10)$$

collisional transitions between nearly degenerate levels by electron and positive ion impact

$$A^{+z-1}(n\ell j) + \left\{{e \atop Z\mu}\right\} \rightarrow A^{+z-1}(n\ell' j') + \left\{{e \atop Z\mu}\right\}, \qquad (11)$$

and transitions between nearly degenerate levels due to ion motion and magnetic fields

$$A^{+z-1}(n\ell j) \underset{B\ \mathrm{mag}}{\rightarrow} A^{+z-1}(n\ell' j') \qquad (12)$$

A statistical view of excited ion level populations is appropriate, the number densities of ions in various excited levels being determined by the balance of populating and depopulating reaction rates. Levels of principal quantum number substantially larger than the upper levels of the observed emitted transitions must be included to allow for cascade contributions. The upper limit is determined properly by collisional ionisation but in practise is mostly influenced by the decay with n of the primary capture processes. The main effect of the particle collisions and magnetic fields is to cause transitions between levels of the same principal quantum number and so these alone are included in the calculations. For ions in high orbital angular momentum states ℓ, induced transitions between whole ℓ state populations are of most importance, whereas, at low ℓ, the transitions between separate j sublevels are important. For these reasons two population models are used, namely

(a) the $n\ell$ picture in which the populations of $n\ell$ levels are calculated and the populations of j sublevels are assumed to be in proportion to their statistical weights,

(b) the $n\ell j$ picture in which the populations of j sublevels are calculated in full. Magnetic field effects are included only in the $n\ell j$ picture.

Turning to the required rates, spontaneous emission rates are calculated using hydrogen-like wave functions.

Electron impact ionisation is calculated in the ECIP approximation[26,27]. Ionisation from highly excited states only is required for this work. There is little guide to this from the many detailed studies of ground state ionisation, however ECIP has the merit of including distant encounters in an impact parameter approximation in the rate coefficient which is relevant to ionisation from highly excited states. It is evident that the treatment adopted in the paper is incomplete in the vicinity of the thermal collision limit since n changing collisional transitions should also be included. The limit is generally substantially above the highest principal quantum shell from which transitions are observed. Consequently most of our results are very insensitive to these details. It is appropriate to view transitions from levels approaching the collision limit as unsuitable for reliable interpretation of charge exchange.

Collisional transitions between nearly degenerate levels play a significant role for the densities, ions and principal quantum shells of concern in JET studies of charge exchange by visible spectroscopy. The transitions are of the form $n\ell \rightarrow n\ell\pm1$ in the $n\ell$ picture and $n\ell j \rightarrow n\ell\pm1_{j,j\pm1}$ in the $n\ell j$ picture and are induced by both electron and positive ion impact. As the transition energies approach zero, ions become relatively more efficient than electrons in causing transitions. Detailed expressions for collision rate coefficients are given in Ref.25 and are adopted here. For greatest precision, rate coefficients for the different positive ions present in the plasma should be combined, weighted by their fractional number densities. Since the cross-section is essentially proportional to Z_μ^2 where Z_μ is the impacting ion charge number, an error less than the intrinsic uncertainty in the cross-sections is introduced by considering only a single ion species to be present of charge Z_{eff}. (Z_{eff} is the usually defined plasma effective ion charge). The rate expressions depend sensitively on the transition energies and so the latter must be evaluated quite precisely. Rates are calculated in the $n\ell j$ picture initially. Since at high ℓ, where the $n\ell$ picture is often most useful, the transitions $n\ell_{\ell+\frac{1}{2}}\rightarrow n\ell+1_{\ell+\frac{1}{2}}$ have line strengths which tend to zero, it is suitable to sum and average over final and initial j states to obtain rate coefficients in the $n\ell$ picture.

It is usual to estimate approximately the levels at which mixing by magnetic fields matter by a simple consideration of static energy level shifts[28]. This is not appropriate for a population treatment in which a detailed balance of rates is followed to obtain actual ion populations in cases where any process may not be fully dominant. A simple theory for transition probabilities for field induced $n\ell j\rightarrow n\ell' j'$ transitions has been developed and is given in appendix B. The magnetic field is effective in causing transitions through the magnetic moment of the ion ($\underline{\mu}.\underline{B}$ in the potential) and through the electrodynamic Stark force ($\underline{v}_A\wedge\underline{B}$) resulting from the cross-field component of the ion velocity $\underline{v}_A$. these rates are to some extent complementary to the collisionally induced rates. It is evident that the field processes matter most at low ℓ in VUV and XUV measurements and that it is the $n\ell j$ picture which is appropriate.

4.3 Charge exchange cross-section models

Theoretical primary charge exchange cross-sections play a principal role in this study, since the final derived impurity ion densities depend absolutely on their reliability. It is unfortunately the case that theoretical charge exchange calculations especially for capture to the highly excited levels of interest here (usually with $n>n_{crit}$ and to separate ℓ states) show variation from one to another. The following general comments may be made. Firstly, the total charge exchange capture cross-section, that is summed over all levels, is the most reliable quantity. This is inferred from the good agreement between different theories and comparisons with experimental beam measurements. Secondly, theories tend to agree on the capture to separate n levels in the vicinity of n_{crit} and indeed on n_{crit} itself, but differ more widely on the behaviour with n significantly above n_{crit}. This is particularly so at low beam energies (E_{beam}<20 keV/amu) where the cross-sections fall rapidly with n. Finally, ℓ distributions of capture show large variations. For these reasons, in Section 4.1 and Appendix A, the solution was organised to base the absolute emission measure on a (limited) sum over n of capture rate coefficients.

We have been concerned to incorporate theoretical data in a number of distinct approximations in our models, both to provide coverage of all relevant beam energies and to allow sensitivity studies of charge exchange approximation dependence. The experimental data from JET allows comment on relative values of cross-sections to different n levels, but not directly on absolute values (Section 5.3). For capture from H(1s) the theoretical charge exchange models used as sources of data are shown in Table V, together with the ions and the nominal beam energy ranges to which they apply. The summed cross-sections to whole n levels are in fact used in our data sets. Table V shows the highest n value, n_{dat} for which explicit data is available. We assume that the cross-section data may be extrapolated above n_{dat} by an expression of the form $\sigma_n \sim n^{-\alpha}$ where α is deduced from the explicit data at n_{dat} and $n_{dat}-1$. The long extrapolation in n necessary for some data sources is a matter of concern especially at beam energy $E_{beam}<40$ keV/amu when the exponent α becomes quite large (>>3). Not all data sources give explicit $n\ell$ resolved capture cross-sections and the variation between these sources may be quite large. We have chosen therefore to implement algebraic forms for the ℓ distribution of the direct capture cross-sections. These forms have been selected to allow representation of explicit data to a reasonable approximation. The forms are shown in Table VI and depend on a parameter ℓ_{cut}. The forms and values for ℓ_{cut} adopted for each model and energy were chosen by fitting near n levels which are the upper levels of main observed transitions. The use of algebraic forms allows sensitivity tests on the effects of ℓ distributions.

For both capture from H(1s) and H(n=2), in the $n\ell j$ picture we have assumed that rate coefficients are in proportion to their statistical weights to j state of the same ℓ. Finally, it should be remarked that the very comprehensive data available for the UDWA approximation has made it the main basis for our systematic experimental studies.

4.4 Parametric studies of effective rate coefficients

Rate coefficients for charge exchange with ground state neutral particles have been calculated for helium, carbon and oxygen visible transitions likely to be observed on JET. The rate coefficients have been evaluated in the $n\ell$ picture and so include cascading and ℓ-mixing. The dependence on energy obtained for typical JET parameters is shown in Fig.17 ($Z_{eff}=2$; $n_{eff}=n_e/Z_{eff}=1.5\text{x}10^{19}$ m^{-3}; $T_i=6$ keV).

The choice of plasma parameters defines the degree of ℓ-mixing. When calculating impurity densities from observed column emissivities, these rates must be evaluated for the actual plasma conditions. As mentioned before, the charge exchange process tends to leave the electron in a high ℓ-state ($\ell \sim n_{crit} \sim Z^{3/4}$), where the branching ratios for $\Delta n=1$ transitions are most favourable. Increasing the mixing among the ℓ-levels therefore decreases the rate coefficients for $\Delta n=1$ transitions from $n>n_{crit}$. Treating the carbon n=8 to n=7 transition as an example, Fig.18 shows as expected that raising the effective ion density increases the degree of ℓ-mixing and decreases the effective rate coefficient. Redistribution among the ℓ-levels is also affected by the effective ion charge (Fig.19) and the ion temperature (Fig.20). For JET parameter range, the degree of ℓ-mixing thus strongly affects the effective rate coefficient and a step transition from no ℓ-mixing to full ℓ-mixing would be inadequate. The main JET analysis has been carried out using this $n\ell$-resolved picture. The numerical values are listed in Appendix C.

4.5 Fast neutral density calculations

In order to extract impurity densities from absolute flux measurements the fast neutral density must be separated from the impurity density in the charge exchange emission measure. This is shown in Appendix D. The result in the simplest case

$$I = q^{CEM}(0)N(A^{+z}|0) \sum_{ij} \frac{\xi_{ij}\, f_j P_i\, \alpha_i}{v_{ij} e E_{ij} \sqrt{\pi}\, w(s_{0i}) \cos \varepsilon_i} \qquad (13)$$

This result is derived in Appendix D. It allows a local impurity density N^{+z} to be derived from a measured column emissivity I. The sum extends over all neutral beams (with power P and width w) and energy components E (with beam fraction f). ξ is the attenuation factor for neutral particles of velocity v. α is the average of the neutral beam shape over the viewing line cross-section area and cos ε is a geometrical factor close to unity (see Appendix D).

Impurity calculations on JET have only been attempted with the vertical line of sight. For this line of sight, α need only be calculated once for each of the neutral beam banks. The ratio of the two coefficients for neutral and tangential beams depends strongly on the exact viewing line position. Shifts as small as 0.5 cm towards one bank or the other can influence significantly the calculation. The most sensitive way of determining this position is by charge exchange flux measurements. Consecutive pulses with identical target plasmas are routinely used to check alignment of the neutral beam sources. By selecting pulses with only normal or tangential bank sources fired, the true position can be estimated from the CX flux ratio. In practice, the viewing line position between the banks can be fixed by this technique to ~1 cm. Measurements inside the vacuum vessel verify this estimate.

The calculation of hydrogen beam attenuation is done numerically. Beam absorption is, in general, due to collisional ionisation by all species and to charge exchange with all plasma ions. Electron impact ionisation cross-sections are taken from Bell et al[39]. They contribute less than 10% of the attenuation. For the ions, in practice, only species contributing significantly to Z_{eff} are important. For JET these are H, He, C and O under normal operating conditions. Also the species are fully ionised except in the edge regions where the attenuation is in any case low. Thus only the ions H^+, He^{+2}, C^{+6} and O^{+8} need to be considered. The cross-sections used are shown in Fig.21. For hydrogen, the two curves are fits to the most recently available experimental data[40-44]. It is worth noting that the fits are significantly different from commonly used cross-sections[45], especially at the beam energies relevant to JET.

The data for He is also primarily experimental[43,46-48], with the low energy range of the ionisation cross-section (below 30 KeV/amu) extended by following the form of the theoretical curve of Janev and Presnyakov[49]. This latter region is not important for net attenuation.

Impurity stopping is found to have a significant role in typical JET plasmas (up to 20% in the beam transmission coefficients). This will be an even larger effect at the higher beam energies planned for future operation. Unfortunately, experimental data for beam stopping on fully stripped carbon and oxygen is sparse. For our analysis we have adopted the theoretical UDWA calculations of Ryufuku[29,30]. These calculations are extended to low energy by the work of Greenland[44] for charge exchange cross-sections and by the theory of Janev and Presnyakov[49] for ionisation cross sections. The high energy fall off of the charge exchange cross sections is given the form predicted by Eichler[50].

The one experimental point for ionisation by C^{+6}[51] and the single sudden approximation point of Salop & Eichler[52] suggest our adopted values may be up to ~ 15% low at the cross-section peak. The results of Olson & Salop[35] and Salop & Olsen[53] are ~ 40% greater than ours at peak.

The required ion densities are calculated by reading the electron density and Z_{eff} from the JET data base and by assuming the carbon to oxygen ratio is three. Sensitivity studies show that significant variation in the C/O ratio does not affect the attenuation calculation. In fact, the presence of a He minority in the discharges, used for minority heating, also does not significantly alter the beam attenuation. Discharges in He with D heating can have more than 25% He concentrations. The beam attenuation predicted for such a JET plasma changes only 5% when performed with 25% He contributing to the Z_{eff} as compared to the reference assumption that the only impurities are C and O. This is because, at the beam energies in these experiments (~ 40 keV/amu), the impurity stopping is dominated by charge exchange which scales approximately as the Z of the ion thus cancelling the effect of density dilution.

4.6 Generalised emission measures and non-hydrogenic ions

There are three alternative primary direct reactions which may be present in the absence of neutral beams or near the edge of JET. These are radiative recombination

$$A^{+z} + e \rightarrow A^{+z-1}(n\ell) + h\nu \tag{14}$$

with an associated 'recombination emission measure' (REM)

$$\int N_e\, N(A^{+z})\, d\ell \tag{15}$$

and effective rate coefficient $q^{REM}(n\rightarrow n')$; collisional excitation from the ground state of the hydrogen-like ion A^{+z-1}

$$A^{+z-1}(1s) + e \rightarrow A^{+z-1}(n\ell) + e \tag{16}$$

with an 'excitation emission measure' (EEM)

$$\int N_e N(A^{+z-1}(1s))\, d\ell \tag{17}$$

and effective rate coefficient $q^{EEM}(n\rightarrow n')$; charge exchange from an excited state of hydrogen present in beams or as thermal hydrogen

$$A^{+z} + H(n=2) \rightarrow A^{+z-1}(n\ell) + H^{+} \tag{18}$$

with an associated 'charge exchange emission measure' (CEM)

$$\int N(H(n=2))\ N(A^{+z})d\ell \qquad (19)$$

and effective rate coefficient $q^{CEM}_{H(n=2)}(n\rightarrow n')$.

Under complex conditions, all these emission measures may simultaneously contribute to the observed column emissivity of a spectrum line. The computer codes have been extended to include these alternative emission measures. A second extension is to allow helium-like and neon-like capturing ions. This has also been implemented. The sources of theoretical data are as follows.

Direct radiative recombination coefficients are calculated using the procedures described by Burgess & Summers[54]. It is evident that the recombination emission measure can only be relevant in a strongly recombining environment in which the ions are present at temperatures lower than expected in ionisation balance. There is no dielectronic recombination for bare nuclei. Theoretical electron impact excitation rate coefficients from the ground state of hydrogen-like ions have been described by Spence and Summers[25]. These are used as the basis for excitation emission measure studies here. For lithium-like and sodium-like ions, data from the compilation of Gordon & Summers[55] is available for low n but extrapolation to high n must be considered quite uncertain. Excitation to j sub levels is assumed to be in proportion to statistical weights.

Charge exchange capture from the excited levels 2s and 2p of thermal hydrogen atoms is a process believed to contribute to observed line emission at the edge of tokamaks under certain circumstances. It is speculated that the capture cross-sections are substantially larger ($\gtrsim$ 8x) than these from H(1s) and that the appropriate n_{crit} is about twice that for H(1s) capture. Theoretical data upon which quantitative calculations can be based and experimental measurements interpreted are extremely limited. We have implemented the 'Eikonal' model[50], which is probably valid for $E_{beam} \gtrsim 40$ keV/amu for capture from H(2s) and H(2p) but there is no model for $E_{beam} < 40$ keV/amu. Low energy charge exchange capture cross-sections from H(n=2) have therefore been inferred by the following procedure.

The classical overbarrier model[56] has been used to obtain n^*_{crit} (a non-integer value) and the principal crossing radius R_x for H(1s), H(n=2) and Li(2s) at 1 KeV/amu. The H(1s) and Li(2s) cross-sections were compared with the data of Fritsch & Lin[62], the ratio being close to 0.85 in both cases. The overbarrier model data was scaled by this factor and divided between the integer n values enclosing n^*_{crit} in proportion to the separations. The cross-section shape with hydrogen energy was assumed to be the same as for capture from Li(2s) but with a displacement in the energy scale. This was inferred from the cross-section maxima with energy for H(1s) and Li(2s) capture. It is clear that only a low level of confidence can be placed on this tentative procedure.

Turning to the population calculation, energy levels in the $n\ell$ and $n\ell j$ picture are calculated for lithium-like ions following the same approximations as Spence & Summers[25]. The Ritz series and polarizabilities of Edlén[57] used there for lithium-like ions extend to the sodium-like case, the relevant parametrizations being given by Edlén[58].

Spontaneous emission rates are calculated in the one-electron approximation using hydrogen-like wave functions in an effective Coulomb field corresponding to the screened nuclear charge of the recombining ion. This is satisfactory for all specific cases studied here with the effective charge equal to the recombining ion charge. More accurate A-values, still in the one-electron approximation are available using the bound-bound Gaunt factor methods[54], but are only expected to be required for transitions from fairly low levels of sodium-like ions at moderate z . We have no practical application for such refinement in charge exchange studies at this stage. $n\ell j$ resolution of the A-values is based on strict LS coupling. Hydrogenic results are used for all other rate coefficients but based on actual energy separations.

In Figs. 22 to 25, some illustrations are given of the generalised operation of the analysis and predictive codes. The calculations are performed in the full j-resolved picture and show the trends of the effective rate coefficients for emission of $\Delta n=1$ and Lyman series. The plasma parameters used to specify the mixing/cascade conditions are given on the figures. They are for a near edge position in the specified JET Pulse. Of note are the curvatures of the effective coefficient variations along the series. These are dependent on the ℓj dependence of the primary capture as modified by mixing. Because of the accidental degeneracy of hydrogen-like ions direct measurement of $n\ell j$ resolved primary capture in experiments is impossible. It is only by the unfolding of observations of multiple series variation of the n shell transition spectrum lines that the direct rates can be obtained. The effective rate coefficients for excitation and (especially) for radiative recombination are much smaller than the charge exchange effective coefficients. Radiative recombination is clearly unimportant in JET. For excitation, the small rate coefficients are compensated by the relatively high emission measures. We return to this point in Section 5.4 in the examination of cold spectrum line features. Charge exchange capture from H(n=2) is strongly resonant (at n~9 for C^{+6} recombination). The source direct capture data as described earlier is of low reliability and so the effective rate coefficients especially for the level above the maximum are quite uncertain.

5. IMPURITY ION DENSITIES IN JET

5.1 Central impurity content

As emphasized in earlier sections, the deduction of absolute impurity densities from observed column emissivities relies on the evaluation of several independent quantities. The reliability of the diagnostic can, however, be tested during transients, when one aspect of the calculation is expected to dominate. For example, the results depend sensitively on the geometry of the observation volume (see Section 2). The fact that no step is apparent on the carbon concentration when the ratio of normal to tangential beam power changes indicates that the position of the line of sight between the two injection lines is properly defined (Fig.26).

In order to obtain absolute impurity densities, much attention was focussed on charge exchange rate coefficients corrected for cascading and ℓ-mixing. Simultaneous observation of two carbon transitions indicates that the experimentally inferred n-dependence of q^{CEM} compares well with the theoretical prediction (see Section 5.2). Similarly, the oxygen concentration was calculated using two different transitions for consecutive pulses corresponding to similar operating conditions of the machine. Those measurements also confirm the consistency of the charge exchange rate coefficients, which differ by approximately a factor 2.5 for these transitions.

The CXRS diagnostic provides information about the impurity content in the plasma centre, which is not directly accessible otherwise. Consequently, there are few other measurements with which to compare. One candidate, however, is the effective ion charge derived from visible bremsstrahlung. Though not a localized measurement, it is heavily weighted to the plasma centre. Z_{eff} is thus computed from CXRS measurements using the two dominant impurities: carbon and oxygen (Fig.27), or carbon and helium (helium discharge, Fig.28), as the case may be:

$$Z_{eff} = 1 + \sum_i Z_i \,(Z_i - 1)\, \frac{N_z}{N_e} \qquad (20)$$

Under most operating conditions, carbon and oxygen are the dominant impurities in JET, and need only to be considered when computing the effective ion charge. High-Z impurities which are usually less than 0.01% may contribute significantly to Z_{eff} only during ICRF heating[59]. For helium discharges similar to the one shown in Fig.28, the oxygen concentration in the plasma centre was found to be very small ($n_o/n_e<0.5\%$) and contributes little to Z_{eff}.

For the measurements shown in Fig.27, JET was operated in a single-null X-point configuration, which gives access to the H-mode regime. In this particular case, the electron density changed by more than a factor of two during the neutral beam injection pulse. The agreement between the Z_{eff} measurements over such a large density range strengthens our confidence in the neutral beams attenuation routine, which depends exponentially on the electron density.

The Z_{eff} comparison was extended to several JET pulses covering a wide range of plasma parameters and auxiliary heating power. The values plotted in Fig.29 were selected one second after the beginning of neutral beam injection. The Z_{eff}

values calculated from CXRS measurements, using the two dominant impurities, are close or only slightly smaller than the value inferred from visible bremsstrahlung.

The same effective ion charge can be obtained from widely different impurity concentrations, depending on the operating conditions of the machine, the ratio of carbon to oxygen concentrations ranging from C/O ~ 1.5-2.5 for 2 MA X-point discharges to C/O ~ 7-10 for 5 MA inner wall discharges (Z_{eff} ~ 2.8 in both cases). Carbon and oxygen concentrations can also be used to determine the evolution of the deuterium concentration during neutral beam injection (Fig.30). Until the H-mode begins, Z_{eff}^{cx} decreases because of the diluting effect of heating neutral beams fuelling. The sharper rise of the electron density on axis at the onset of the H-mode beams seems mainly due to an increase of the central impurity content. It is often observed that the rate of increase of the deuterium density calculated from oxygen and carbon measurements is little affected by the H-mode regime. The carbon and oxygen concentration therefore increase steadily during H-mode, at the expense of the deuterium concentration.

The behaviour of carbon and oxygen densities depends markedly on the operating conditions of the machine, as revealed by the analysis of two consecutive pulses shown on Fig.31 (2 MA, limited on inner wall of the vessel) and Fig.32 (2 MA, single null X-point configuration). It is usually observed on JET that the ratio of carbon to oxygen densities decreases slightly during neutral beam injection for discharges limited on the inner wall of the vessel, but increases during

X-point operation. In the L-mode regime, the oxygen density is comparable for both operating conditions, but the carbon density is significantly higher when the plasma is limited on the inner wall (coated with carbon tiles). The H-mode regime clearly appears as a sharp increase of the impurity content.

5.2 The experimental assessment of charge exchange effective rate coefficients

Instead of monitoring charge exchange lines from different impurities as in the previous section, two transitions of the same element can be observed simultaneously using the dual spectrometer arrangement. The viewing geometry and the emission measure being the same, the ratio of the column emissivities should reflect the ratio of the effective charge exchange rate coefficients. The following combinations of carbon transitions were selected:

(i) n=8 to n=7 (5290.5 Å); n=10 to n=8 (4498.8 Å)
(ii) n=8 to n=7 (5290.5 Å); n=11 to n=9 (6200.7 Å)
n=13 to n=10 (6198.1 Å)

In all cases, the charge exchange signature could be identified by comparing spectra collected during and after neutral beam injection. On the assumption that similar temperatures for both hot components is an indication of a reliable fit, then

$$\frac{q^{CEM}(10\rightarrow 8)}{q^{CEM}(8\rightarrow 7)} \simeq 0.15 \pm 0.02$$

The error corresponds to the scatter of the experimental points and does not take into account the uncertainty attached with the calibration of both detection systems. In case (ii), the two transitions were barely separable because of poor signal strength and high impurity ion temperature. Only an upper limit on the ratio of rate coefficients can be given:

$$\frac{q^{CEM}(11-9) + q^{CEM}(13-10)}{q^{CEM}(8-7)} \leq 0.10$$

The comparison in Table VII with predictions from different theoretical models indicate that the experimental ratios are only slightly higher than the predicted values. Following the procedure outlined in section 4.1, the measured column emissivities for carbon 8→7 and 10→8 transitions are used to compare the experimental and theoretical estimates of the primary charge exchange rates. As seen in Table VIII, the dependence on the quantum shell number n inferred from the experiment ($\sim n^{-2.5}$) is very close to the theoretical prediction ($\sim n^{-3.0}$). Measurements of other transitions would be necessary for a more definite analysis.

The oxygen 10→9 and 9→8 transitions have also been monitored using consecutive discharges corresponding to similar operating conditions of the machine. The ratio of the rate coefficients is listed in Table VI, together with the theoretical prediction. The measurement is in good agreement with the model adopted in this paper (UDWA).

5.3 Interpretation of the cold feature of C VI lines

Throughout the paper, the hot central charge exchange feature has been separated from interfering cold features in an empirical experimental manner. A mechanism for the production of these features would add confidence to the procedure, allow refinement of the separation process and possibly lead to new edge plasma diagnostic information. For these reasons, some effort has been devoted to understanding the cold features. This is still at a preliminary stage and will be published fully in a separate paper. In the present work, we wish to summarise the phenomena briefly as they appear on JET and to show by the analysis of one case what the probable mechanisms are. It is hoped that this will be of assistance in studies in other fusion plasmas.

The following observations are suggestive. A single cold feature is observed with the hot feature in carbon charge exchange lines. The cold feature alone is observed with the passive viewing line and before and after neutral beam injection. No cold feature could be identified on the oxygen spectra. Furthermore, only a cold feature is observed at 4658 Å, which is the position of the Be^{+3} (6→5) transition. Noting that JET has no beryllium or neon impurity content at this time, these facts indicate that coincidence of emission from lithium-like systems plays a role. On the other hand the helium hot charge exchange features appear to have two cold components. Since there is no beryllium, this indicates that some true He^{+1} transitions play a role. Noting the cold feature temperatures and the high transitions observed, we have postulated impact excitation of hydrogen-like and lithium-like ions and charge exchange recombination of base nuclei and helium-like ions from thermal hydrogen in the n=2 level as likely mechanisms.

We have investigated C^{+5} (8→7) in a limiter discharge. There was no neutral beam injection so only the cold feature is present. Absolute concentrations of carbon and oxygen were assumed in the ratio 3:1 as is typical of limiter discharges. The radial distribution of the absolute densities of the ionisation stages of carbon and oxygen were inferred from an impurity transport code[20], using the observed electron temperature and density radial profiles and matching to boundary probe data. Neutral hydrogen density radial variation was inferred from neutral particle analyser data via a diffusion model[60]. The excited n=2 level population was deduced assuming fully mixed 2s and 2p populations and using recent excitation data[61]. Effective rate coefficients for the species and mechanisms were calculated using the generalised codes described in Section 4.6. The results are summarised in Table IX. The theoretical calculation yields 60% of the observed line emission, with the following individual contributions from the different mechanisms considered

C^{+6} charge exchange recombination	6.0%
O^{+6} charge exchange recombination	0.7%
C^{+5} impact excitation	9.5%
O^{+5} impact excitation	42.3%
Total	58.5%

Some caution is required in assessing this result. Firstly the substantial uncertainties in distributions and rate coefficients used suggest that probably the relevant mechanisms have been identified but the balance between mechanisms will alter markedly depending on viewing lines and machine operating conditions. Evidently a more systematic set of observations and analysis of the cold features on JET are required before final conclusions can be reached. However, the separated hot feature analysis seems justified.

6. CONCLUSIONS

The results of visible charge exchange recombination spectroscopy on JET have been used to deduce temperature, rotation velocity and density of the dominant low-Z impurities in the plasma centre from absolutely calibrated measurements of Doppler widths, Doppler shifts and intensities of recombination line radiation emitted in the visible spectrum. It has been shown that the restriction to the visible part of the spectrum introduced by the use of fibre links, and the consequent necessity to use intensities from highly excited quantum shells has not constrained the analysis. By contrast, absolute calibration procedures are facilitated considerably and can be carried out routinely. The use of fibre links to remote spectral instruments is an essential feature of the future active phase of JET where enhanced neutron bombardment inhibits the operation of spectrometers and detectors in the immediate vicinity of the torus.

The spectra are observed to be composite profiles consisting of a broad charge exchange feature representing the plasma core and additional narrow components excited in the plasma boundary. Our results have demonstrated that the various features can be unambiguously separated by applying multi-Gaussian fit routines. It is suggested that the identification of the narrow edge components is quite complex. In the case of the dominant carbon and helium transitions our results indicated that more than one sub feature involving different excitation mechanisms such as electron impact and charge exchange with a cold dense neutral hydrogen shell at the plasma boundary may constitute the cold component.

Ion temperatures derived from the Doppler widths of five different CX transitions from helium, carbon and oxygen have been analysed and agreed within 10%. No systematic mass dependence within the investigated range of M=4 amu and m=16 amu was found.

Central impurity density calculation from absolute charge exchange column emissivities has been implemented as a routine diagnostic on JET during neutral beam heating. It involves the calculation of local fast neutral particle density and relies on atomic physics models for the effective rate coefficients. The uncertainties attached to those quantities are difficult to assess. Our results have shown that modelling of the cascading and redistribution processes following charge capture to actual plasma parameters leads to consistent results in low-Z impurity ion densities. Comparison of effective ion charge values based on dominant low-Z impurities such as carbon and oxygen to independent measurements of the effective ion charge by visible bremsstrahlung indicated that the concentrations of oxygen and carbon in the plasma centre determined by charge exchange spectroscopy are in a reasonable range. The two values of effective ion charge were shown to agree within estimated error bars of both diagnostics and to follow the same temporal development during distinctive changes of heating power, ion density and temperature.

The present results of the charge exchange spectroscopy diagnostic have opened a range of future applications and further investigations. A multi chord viewing line system intersecting the neutral heating beams at various radii is presently being commissioned. This system will enable measurement of radial profiles of ion temperature, ion density and bulk plasma rotation. It is intended to exploit the diagnostic potential of the Balmer Alpha spectrum using lines of sight not perpendicular to the beams and thus measure directly the deuterium temperature and density during beam injection. Following the detail of the narrow excited beam components along the path through the plasma will give information on beam attenuation.

A comparison of different ion temperature diagnostics on JET has shown the need for spatially resolved measurements including an investigation of temperature anisotropy and velocity shear effects. Possible effects of impurity masses on derived temperatures could be studied by extending our present range of low-Z impurities to neon and argon.

A further aim is to investigate the helium charge exchange recombination spectrum as a possible candidate for future alpha particle diagnosis. A first step for this programme will be to extend the presently observed thermal spectra far into high energy wings during RF minority heating.

The models for effective rate coefficient calculation, theoretical and experimental direct capture coefficient comparison and spectral emission prediction developed and exploited in the paper of of some generality. They take the form of interactive FORTRAN computer codes which are available for a wide range of applications.

APPENDIX A

Emission measure model procedures

The Appendix addresses the matrix manipulation required to deduce the emission measure, compare experimental and theoretical primary rate coefficients, and predict line intensities, based on a limited set of observed column emissivities.

Suppose that experimental column emissivity data is available for spectrum lines with upper principal quantum levels n with $n_{min} \leq n \leq n_{max}$. For simplicity assume all levels between n_{min} and n_{max} are represented. Let the total number of principal quantum levels in the model be n_{tot}. Let the population density of ions in the level $n\ell j$ be $N_{n\ell j}$ in the $n\ell j$-picture and in the level $n\ell$ be $N_{n\ell}$ in the $n\ell$-picture. The vector of populations for the n shell is $\underline{N}^{(n)}$.

Consider firstly populations of levels n with $n_{max} \leq n \leq n_{tot}$. Let the primary direct rate coefficient vector to level n be $\underline{q}^{(n)}$. We assume that theory may be used without serious error to give

$$\underline{q}^{(n)} = q^{(n)} \; \underline{f}^{(n)}$$

$$\text{and } \underline{q}^{(n)} = \underline{q}^{(n_{max})} \left(\frac{q^{(n)}}{q^{(n_{max})}}\right)^{THEOR} \qquad \text{(A-1)}$$

Thus $q^{(n)}$ is the total primary rate coefficient to the level n and $\underline{f}^{(n)}$ is the vector of fractions to the separate ℓ or ℓj levels depending upon the resolution choice. All the $\underline{f}^{(n)}$'s for $n_{min} \leq n \leq n_{tot}$ are obtained from theory. Without loss of generality consider charge exchange recombination from H(1s) as the primary process. Then the population of level n_{tot} is given by

$$\underline{\underline{M}}^{(n_{tot},n_{tot})}\ \underline{N}^{(n_{tot})} = n_H N_+\ q^{(n_{max})} \left(\frac{q^{n(tot)}}{q^{(n_{max})}}\right) \text{THEOR}\ \underline{f}^{(n_{tot})} \tag{A-2}$$

Likewise for level n

$$\underline{\underline{M}}^{(n,n)}\ \underline{N}^{(n)} = N_H N_+\ q^{(n)} \left(\frac{q^{(n)}}{q^{(n_{max})}}\right) \text{THEOR}\ \underline{f}^{(n)} + \sum_{n'=n+1}^{n_{tot}} \underline{\underline{C}}^{(n,n')}\ \underline{N}^{(n')} \tag{A-3}$$

where $\underline{\underline{C}}$ is the direct cascade matrix between n' and n. The $\underline{\underline{M}}$'s are tridiagonal matrices with off-diagonal elements composed of collisional and field induced redistribution rates of the form $n\ell \rightarrow n\ell\pm1$ or $n\ell j \rightarrow n\ell\pm1 j'$ (negatively signed) and on-diagonal elements composed of sums of the inverse reaction rates, inverse radiative lifetimes and ionisation rates of the levels. The latter may be introduced to allow useful reduction near the ionisation limit. These matrix equations may be inverted recursively downwards to obtain the vectors $\underline{W}^{(n,n_{max})}$ such that

$$\frac{\underline{N}^{(n)}}{N_H N_+} = q^{(n_{max})}\ \underline{W}^{(n,n_{max})} \tag{A-4}$$

In effect this expresses all the populations of levels ≥ n_{max} in terms of the two unknown quantities $q^{(n_{max})}$ and $N_H N_+$. Consider now populations of levels $n_{min} \leq n < n_{max}$. The populations of level $n_{max}-1$ is given by

$$\underline{\underline{M}}^{(n_{max}-1,n_{max}-1)}\ \frac{\underline{N}^{(n_{max}-1)}}{N_H N_+} = q^{(n_{max}-1)}\ \underline{f}^{(n_{max}-1)} - q^{(n_{max})} \left[\sum_{n'=n_{max}}^{n^{tot}} \underline{\underline{C}}^{(n_{max},n')}\ \frac{\underline{N}^{(n)}}{N_H N_+} \right] \qquad \text{(A-5)}$$

Inverting, the solution for $\frac{\underline{N}^{(n_{max}-1)}}{N_H N_+}$ may be written

$$\frac{\underline{N}^{(n_{max}-1)}}{N_H N_+} = q^{(n_{max}-1)}\ \underline{W}^{(n_{max}-1,n_{max}-1)} - q^{(n_{max})}\ \underline{W}^{(n_{max}-1,n_{max})} \qquad \text{(A-6)}$$

with unknowns $N_H N_+, q^{(n_{max}-1)}$ and $q^{(n_{max})}$.

This process is repeated so that for arbitrary n

$$\frac{\underline{N}^{(n)}}{N_H N_+} = \sum_{n'=n}^{n_{max}} q(n')\ \underline{W}^{(n,n')} \qquad \text{(A-7)}$$

If we denote the observed column emissivity of the line based on upper level n by $I^{(n)}$ $(n_{min} \leq n \leq n_{max})$, then

$$I^{(n)} \simeq \sum_{n'=n}^{n_{max}} \left[\int N_H N_+ \, d\ell \ q^{(n')} \right] B^{(n,n')} \qquad \text{(A-8)}$$

where the B's are derived from the W's. Inversion using the observed $I^{(n)}$'s yields the quantities

$$\left(\int N_H N_+ \, d\ell \right) q^{(n)} \text{ for } n_{min} \leq n \leq n_{max}.$$

The assumption

$$\sum_{n=n_{min}}^{n_{max}} \left(q^{(n)} \right)^{THEOR} = \sum_{n=n_{min}}^{n_{max}} q^{(n)} \qquad \text{(A-9)}$$

gives finally the emission measure $\int n_H N_+ \, d\ell$ and the experimental rate coefficients $q^{(n)}$.

The column emissivities of arbitrary lines n with $n_{min} \leq n \leq n_{tot}$ may be reconstructed theoretically from the deduced emission measure $q^{(n)}$'s and the various matrices.

APPENDIX B

Rate coefficients for level mixing by magnetic fields

For magnetic induction $\underline{B}$ and in ion velocity $\underline{v}_i$, transforming to the ion frame of reference gives a perturbation to the field free Hamiltonian

$$H_{mag.} + H_{dyn.} = \underline{\mu}.\underline{B} + \frac{e}{c}\,\underline{v}_i \wedge \underline{B}.\underline{r} \qquad \text{(B-1)}$$

where $\underline{r}$ is the electron co-ordinate vector relative to the ion frame and $\underline{\mu} = -\frac{e}{2m_e c}(\underline{L}+2\underline{S})$ is the magnetic moment. $\underline{L}$ and $\underline{S}$ are the usual orbital angular momentum and spin operators for the electron.

For one electron states $\psi(n\ell jm)$ and $\psi'(n\ell'j'm')$, with z-axis orientated along the direction $\underline{B}$

$$\langle n\ell jm|-\underline{\mu}.|n'j'm'\rangle = \frac{eB\hbar}{2m_e c}\{m\delta_{\ell jm,\ell'j'm'} + \delta_{\ell m,\ell'm'}.(-1)^{j'-\ell'\frac{1}{2}}\sqrt{\frac{3}{2}}(2j'+1)^{\frac{1}{2}}\,C^{j'1j}_{m'om}\,W(\tfrac{1}{2}\tfrac{1}{2}jj';1\ell)\} \qquad \text{(B-2)}$$

and

$$\langle n\ell jm|\frac{e}{c}\,\underline{v}_i\wedge\underline{B}.\underline{r}|n\ell'j'm'\rangle = \frac{ev_iB}{c}\sin\Theta_i\,\frac{1}{\sqrt{2}}(-1)^{\ell+j'}\sqrt{(2\ell'+1)(2j'+1)}\; C^{\ell'1\ell}_{ooo}\,W(\ell\ell'jj';1\tfrac{1}{2})\;\langle n\ell|r|n\ell'\rangle\{e^{i\phi_i}\,C^{j'1j}_{m'1m} + e^{-i\phi_i}\,C^{j'1j}_{m'-1m}\} \qquad \text{(B-3)}$$

where Θ_i and ϕ_i are the polar angles of the ion velocity relative to the direction $\underline{B}$. Assume that m states are equally populated in the plasma. Then summing and averaging over final and initial m states gives for

$\underline{n\ell j\rightarrow n\ell j'}$

$$\frac{1}{(2j+1)}\sum_{m,m'}\left|\langle H_{mag}\rangle\right|^2 = \left(\frac{eB\hbar}{2m_e c}\right)^2 \cdot\frac{3}{2}\cdot\frac{1}{3}\cdot(2j'+1)\ W^2(\tfrac{1}{2}\tfrac{1}{2}jj';1\ell) \tag{B-4}$$

and for

$\underline{n\ell j\rightarrow n\ell' j'}$

$$\frac{1}{(2j+1)}\sum_{m,m'}\left|\langle H_{dyn}\rangle\right|^2 = \left(\frac{ev_iB}{c}\sin\theta_i\right)^2 (2\ell'+1)(2j'+1) \left[C^{\ell'1\ell}_{o\ o\ o}\ W(\ell\ell'jj';1\tfrac{1}{2})\langle n\ell|r|n\ell'\rangle\right]^2 \tag{B-5}$$

where $\langle n\ell|r|n\ell'\rangle = \frac{3}{2z_1}\ n\sqrt{n^2-\ell_>^2}\ a_o$ with $\ell_>=\max(\ell,\ell')$ and z_1 the effective ion charge

If the perturbation acts for time τ between interruptions, the interruption frequency is $\frac{1}{\tau}$ and the transition probability becomes

$$\frac{4}{\hbar^2}\left(\frac{h}{\Delta E_{n\ell j,n\ell'j'}}\right)^2 \frac{\sin^2\left(\frac{\Delta E_{n\ell j,n'\ell'j'}\tau}{\hbar}\right)}{\tau}\ \frac{1}{(2j+1)}\sum_{m,m'}\left|\langle H_{\left\{\begin{smallmatrix}dyn\\mag\end{smallmatrix}\right\}}\rangle\right|^2 \tag{B-6}$$

in first order time dependent perturbation theory.

If $\frac{\Delta E\tau}{\hbar} \ll 1 \qquad \frac{\sin^2\frac{\Delta E\tau}{\hbar}}{\tau} \simeq \left(\frac{\Delta E}{\hbar}\right)^2\tau$

and if $\frac{\Delta E\tau}{\hbar} > .52 \qquad \left\langle\frac{\sin^2\frac{\Delta E\tau}{\hbar}}{\tau}\right\rangle_{av} \simeq \frac{1}{2\tau}$

Thus the transition probability in general is approximately

$$\frac{4}{\hbar^2}\left(\frac{\hbar}{\Delta E_{n\ell j,n\ell' j'}}\right)^2 \min\left\{\begin{matrix}\left(\frac{\Delta E_{n\ell j,n\ell' j'}}{\hbar}\right)^2\tau \\ \frac{1}{2\tau}\end{matrix}\right\} \frac{1}{(2j+1} \sum_{m,m'} \left|H_{\left\{\begin{smallmatrix}dyn\\ mag\end{smallmatrix}\right\}}\right|^2 \qquad (B-7)$$

The expression for $\frac{1}{(2j+1)} \sum_{m,m'} \left|H_{dyn}\right|^2$ may be averaged over uniformly distributed pitch angles by replacing $\sin^2\theta_i$ by $\frac{4}{3}$ and averaged over a Maxwellian ion distribution by replacing v_i^2 by $\frac{3kT_i}{m_i}$.

It remains to consider the choice of coherence time τ. Possible choices are

(a) Radiative lifetime

(b) Magnetic fluctuation time

(c) Toroidal rotation time

(d) Ion-ion collision pitch angle re-orientation time.

The effective τ is the smallest of these. Under most circumstances, this is the radiative lifetime for spontaneous emission (a).

Field mixing transition rates are derived here in outline for completeness. Detailed application is reserved for later studies of VUV emission involving low angular momentum states. It is anticipated that some adjustment particularly of the strongly coupled regime will be required.

APPENDIX C

Tabulations of effective charge exchange rate coefficients

Charge exchange effective rate coefficients are listed for some carbon, oxygen and helium transitions used on JET. Table X gives the dependence on injected neutral particle energy for typical JET parameters ($Z_{eff} \simeq 2$, $n_{eff} = n_e/Z_{eff} \simeq 1.5 \times 10^{19} m^{-3}$, $T_i \simeq 6$ keV). The effective rate coefficients are also influenced by the actual plasma conditions via ℓ-mixing. Tables XI, XII and XIII show the effect of redistribution among the ℓ-levels as a function of the effective ion density, the ion temperature and the effective ion charge.

APPENDIX D

Detailed fast neutral density calculations

In the following calculation, the fast neutral density is evaluated for an arbitrary complex geometry. With some simplifications valid for our particular experimental configuration, Eq.(13) in Section 4.5 is deduced.

Consider a single monoenergetic neutral beam and a viewing line with geometry as given in Fig.33. The charge exchange column emissivity is

$$I = \frac{\int_V d^3\ell\ q^{CEM}(\underline{\ell})\ N(H|\underline{\ell})\ N(A^{+z}|\underline{\ell})}{\int_A d\ell_2\ d\ell_3} \qquad \text{(D-1)}$$

where V and A are the volume and cross sectional area of the viewing line as defined by the collecting optics. The effective rate coefficient is separated from the integral by picking a reference location (0 in Fig.33) and defining a normalised shape function

$$\psi_q(\underline{\ell}) = q^{CEM}(\underline{\ell}) \ / \ q^{CEM}(0) \qquad \text{(D-2)}$$

Thus

$$I = q^{CEM}(0)\ \frac{1}{A}\ \int_V d^3\ell\ \psi_q(\underline{\ell})\ N(H|\underline{\ell})\ N(A^{+z}|\underline{\ell}) \qquad \text{(D-3)}$$

and if $\psi_q(\underline{\ell}) = 1$ throughout the viewing volume then the separation from the emission measure is complete. Similarly separating $N(H|\underline{\ell})$ and $N(A^{+z}|\underline{\ell})$:

$$I = q^{CEM}(0)\ N(H|\ell_0)\ N(A^{+z}|0)\ L \qquad \text{(D-4)}$$

where

$$L = \frac{1}{A}\ \int_V d^3\ell\ \psi_q(\underline{\ell})\ \psi_H(\underline{\ell})\ \psi_Z(\underline{\ell}) \qquad \text{(D-5)}$$

is an effective length which is determined primarily by the viewing area and the profile of the neutral beams. Note that the fast hydrogen density has been normalised to a different point which will be unique to each neutral beam.

Calorimeter measurements have shown[22] that the beam profile can be well approximated by a gaussian with constant divergence from a point source. Thus, in beam co-ordinates,

$$N(H) = \frac{n_o}{\pi w^2(s)} e^{-r^2/w^2(s)} e^{-\int_A^S n\sigma dx} \qquad (D\text{-}6)$$

where

$$n_o = \frac{P}{veE}$$

$$w(s) = s \tan \gamma$$

and γ is the beam divergence as deduced from the calorimeter measurements. Separating Eq.(D-6) into reference density and shape function gives

$$N(H|\ell_o) = \frac{n_o}{\pi w^2(s_o)} e^{-\delta^2/w^2(s_o)} e^{-\int_A^{\ell_o} n\sigma dx} \qquad (D\text{-}7)$$

$$\psi_H(\underline{\ell}) = \frac{w^2(s_o)}{w^2(s)} \frac{e^{-\int_A^S N\sigma dx}}{e^{-\int_A^{\ell o} N\sigma dx}} e^{\delta^2/w^2(s_o)} e^{-r^2/w^2(s)} \qquad (D\text{-}8)$$

We now assume that the viewing volume as defined by the collecting optics and the beam width is small so that the beam width and attenuation are approximately constant in this volume. ψ_H then simplifies to

$$\psi_H(\underline{\ell}) = e^{-(r^2-\delta^2)/w^2(s_o)} \qquad (D\text{-}9)$$

Again, assuming a narrow viewing line, the other profile functions are assumed to depend only on ℓ_1. In fact, we will assume that the rate coefficient profile is flat (ie $\psi_q(\ell_1)=1$). Thus,

$$L = \frac{1}{A} \int_A d\ell_2 d\ell_3 \int_{-\infty}^{\infty} d\ell_1 \; \psi_Z(\ell_1) \; e^{-(r^2-\delta^2)/w^2(s_o)} \tag{D-10}$$

Now applying the co-ordinate transformation

$$r^2 = (\delta-\ell_3)^2 + (\ell_1-\ell_o)^2 \cos^2\varepsilon$$

gives

$$L = e^{\delta^2/w^2(s_o)} \int_{-\infty}^{\infty} d\ell_1 \; \psi_Z(\ell_1) \; e^{-(\ell_1-\ell_o) \cos^2\varepsilon/w^2(s_o)} \; \alpha \tag{D-11}$$

where

$$\alpha = \frac{1}{A} \int_A d\ell_2 d\ell_3 \; e^{-(\delta-\ell_3)^2/w^2(s_o)} \tag{D-12}$$

If the divergence of the viewing line is small over the beam width then α is not a function of ℓ_1 and can be integrated once numerically and treated as a coefficient in the analysis. Also, if ψ_Z is constant over the beam width then the remaining integral can be performed analytically:

$$L = \alpha \; \psi_Z(\ell_o) \; \frac{\sqrt{\pi} \; w(s_o)}{\cos \varepsilon} \; e^{\delta^2/w^2(s_o)} \tag{D-13}$$

This method can be easily generalised into several neutral beams, i, each with three energy components, j, by using the following transformations

$$\delta \rightarrow \delta_i; \; \varepsilon \rightarrow \varepsilon_i; \; \ell_o \rightarrow \ell_{oi} : \; s_o \rightarrow s_{oi} : \; A \rightarrow A_i$$

$$P \rightarrow f_j P_{ij}; \; E \rightarrow E_{ij} = E_i/J; \; v \rightarrow v_{ij}; \; \sigma \rightarrow \sigma_{ij}$$

giving

$$I = q^{CEM}(\emptyset) \; N_Z(A^{+Z}\emptyset) \sum_{i,j} N_j(H|\ell_{oi}) \; L_{ij} \tag{D-14}$$

$$N_j(H|\ell_{oi}) = \frac{\xi_{ij}\, f_j\, P_i}{v_{ij} e\, E_{ij}\, \pi\, w^2(s_{oi})}\, e^{-\delta_i{}^2/w^2(s_{oi})} \qquad (D\text{-}15)$$

$$L_{ij} = \alpha_i\, \psi_Z(0)\, \frac{\sqrt{\pi}\, w(s_{oi})}{\cos\, \varepsilon_i}\, e^{\delta_i{}^2/w^2(s_{oi})} \qquad (D\text{-}16)$$

$$\xi_{ij} = e^{-\int_{A_i}^{\ell_{oi}} N\sigma_{ij} dx} \qquad (D\text{-}17)$$

In the simplest case where there is only one beam or where the beams are closely spaced so that ψ_Z is constant for all beams, the reference point can be chosen to be in that interval $(\ell_o - 0)$ and

$$I = q^{CEM}(0)\; N(A^{+Z}|0) \sum_{ij} \frac{\xi_{ij}\, f_j P_i\, \alpha_i}{v_{ij} e E_{ij} \sqrt{\pi}\, w(s_{oi})\, \cos\varepsilon_i} \qquad (D\text{-}18)$$

ACKNOWLEDGEMENTS

The authors wish to acknowledge the collaboration of the JET staff and especially the diagnosticians who have made their data available to us.

We are in particular indebted to P D Morgan for his constant help and expertise on visible bremsstrahlung measurement. The assistance of M J Forrest (survey spectroscopy) and M L Watkins, P Stubberfield and R Hemsworth (neutral beam data) is much appreciated. Special thanks are due to A Talbot for the development of the data acquisition software. We wish to thank W Engelhardt and K Behringer for their continuous support and numerous suggestions. Many stimulating and very constructive discussions with N J Peacock are greatly appreciated. Two of us (AB and LDH) acknowledge support from the Natural Sciences and Engineering Research Council of Canada.

REFERENCES

1 R J Fonck, R J Goldston, R Kaita, D E Post, Appl. Phys. Lett. 42, 239 (1983)

2 R J Groebner, N H Brooks, K H Burrell, L Rottler, Appl. Phys. Lett. 43, 920 (1983)

3 G A Cottrell, Nucl. Fusion 23, 1689 (1983)

4 S Suckewer et al., Appl. Phys. Lett. 45, 236 (1984)

5 E L Berezovskij, M M Berezovskaya, A B Izvozchikov, V A Krupin, V A Rantsev-Kartinov, Nucl. Fusion 25, 1495 (1985)

6 M von Hellermann et al., 13th European Conference on Controlled Fusion and Plasma Physics, Schliersee, RFG vol.1, 120 (1986)

7 R C Isler, L E Murray, Appl. Phys. Lett. 42, 355 (1983)

8 N C Hawkes, N J Peacock, Nucl. Fusion 25, 971 (1985)

9 G Gammel, R Kaita, R Fonck, K Jaehnig, E Powell, Rev. Sci. Instrum. 57, 1800 (1986)

10 R P Seraydarian, K H Burrell, N H Brooks, R J Groebner, C Kahn, Rev. Sci. Instrum. 57, 155 (1986)

11 K H Burrell, R J Groebner, H St John and R P Seraydarian, submitted to Nuclear Fusion (1987)

12 A N Zinov'ev, A A Korotko, E R Krzhizhanovskij, V V Afrosimov, Yu S Gordeev, JEPT Lett. 32, 539 (1980)

13 R C Isler et al., Phys. Rev. A 24, 2701 (1981)

14 R J Fonck et al., Phys. Rev. Lett. 49, 737 (1982)

15 B P Duval, N C Hawkes, S J Fielding, R C Isler, N J Peacock, Nucl. Instrum. and Methods in Phys. Research B 9, 689 (1984)

16 M G von Hellermann, A Boileau, L D Horton, H P Summers, N J Peacock, Proceedings of the Workshop on Basic and Advanced Fusion Plasma Diagnostic Techniques, Varenna, Italy, vol.1, 120 (1986)

17 M von Hellermann, et al., 14th European Conference on Controlled Fusion and Plasma Physics, Madrid, Spain, vol.3, 1260 (1987)

18 P G Carolan, et al., Phys.Rev. A 35, 3454 (1987)

19 K Ida, R J Fonck, S Sesnic, R A Hulse, B Leblanc, Phys. Rev. Lett. 58, 116 (1987)

20 K H Behringer et al., Nucl. Fusion 26, 751 (1986)

21 G Duesing et al., Plasma Phys. Controlled Fusion 28, 1429 (1986)

22 R Hemsworth, Private communication (1986)

23 P D Morgan et al., Rev. Sci. Instrum. 56, 862 (1985)

24 P G Carolan, M J Forrest, N C Hawkes, N J Peacock, 12th European Conference on Controlled Fusion and Plasma Physics, Budapest, Hungary vol.1, 263 (1985)

25 J Spence, H P Summers, J. Phys. B 19, 3749 (1986)

26 A Burgess, Proceedings of Symposium on Atomic Collision Processes in Plasmas, UKAEA Culham Laboratory Report CLM-4818 (1964)

27 H P Summers, Rutherford Appleton Laboratory Report IM-367 (1974)

28 R J Fonck, D S Darrow, K P Jaehnig, Phys. Rev. A 29, 3288 (1984)

29 H Ryufuku, T Watanabe, Phys. Rev. A 18, 2005 (1978)

30 H Ryufuku, JAERI Report JAERI-M-82-031 (1982)

31 H Ryufuku, Phys. Rev. A 25, 720 (1982)

32 D Rapp, J. Chem. Phys. 61, 3777 (1974)

33 W Fritsch, Phys. Rev. A 30, 3324 (1984)

34 W Fritsch, C D Lin, Phys. Rev. A 29, 3034 (1984)

35 R E Olson, A Salop, Phys. Rev. A 16, 531 (1977)

36 R E Olson, Phys. Rev. A 24, 1726 (1981)

37 T A Green, E J Shipsey, J C Browne, Phys. Rev. A 25, 1364 (1982)

38 E J Shipsey, T A Green, J C Browne, Phys. Rev. A 27, 821 (1983)

39 K L Bell, H B Gilbody, J G Hughes, A E Kingston, F J Smith, UKAEA Culham Laboratory Report CLM-R216(1982)

40 G W McClure, Phys. Rev. 148, 47 (1966)

41 A B Wittkower, G Riding, H B Gilbody, Proc. Phys. Soc. 89, 541 (1966)

42 W L Fite, R F Stebbings, D G Hummer, R T Brackman, Phys. Rev. 119, 663 (1960)

43 M B Shah, H B Gilbody, J. Phys. B 14, 2361 (1981)

44 P T Greenland, UKAEA Harwell Laboratory Report AERE-R11281 (1984)

45 R L Freeman, E M Jones, UKAEA Culham Laboratory Report CLM-R137 (1974)

46 M B Shah, H B Gilbody, J. Phys. B 11, 121 (1978)

47 A Anderson, P Hvelplund, ICPEAC XI Proceedings, p 256 (1979)

48 W L Nutt, R W McCullogh, K Brady, M B Shah, H B Gilbody, J. Phys. B 11. 1457 (1984)

49 R K Janev, L P Presnyakov, J. Phys. B 13, 4233 (1980)

50 J Eichler, Phys. Rev. A 23, 498 (1981)

51 M B Shah, H B Gilbody, J Phys. B 16, 1449 (1983)

52 A Salop, J Eichler, J Phys. B 12, 257 (1979)

53 A Salop, R E Olson, Phys. Rev. A 16, 1811 (1977)

54 A Burgess, H P Summers, Mon. Not. R. Astr. Soc. 226, 257 (1987)

55 H Gordon, H P Summers, UKAEA Culham Laboratory Report CLM-R250 (1985)

56 R Mann, F Folkmann, H F Beyer, J. Phys. B 14, 1161 (1981)

57 B Edlén, Physica Scripta 19, 255 (1979)

58 B Edlén, Physica Scripta 17, 566 (1978)

59 K Behringer et al., 11th International Conference on Plasma Physics and Controlled Nuclear Fusion Research, Kyoto, Japan (1986)

60 S Corti et al., 12th European Conference on Controlled Fusion and Plasma Physics, Budapest, Hungary vol.1, 291 (1985)

61 J Callaway, M R C McDowell, Comments on At. and Molec. Phys. 13, 19 (1983)

62 W Fritsch, C D Lin, J. Phys. B 17, 3271 (1984)

TABLE I

Ion	Δn = 1				Δn = 2,3				T_e
	Trans	Weighted mean wavelength	Component Spread	Emission measure	Trans	Weighted mean wavelength	Component Spread	Emission measure	
		Å	Å	10^{19}cm^{-5}		Å	Å	10^{20}cm^{-5}	eV
He^{+}	4-3	4685.24	4684.91-4685.45	27.5	5-3 6-4 7-4	3202.79 6559.44 5410.98	3202.65-3202.87 6559.11-6559.55 5410.75-5411.06	8.97 21.2 47.6	3700
Be^{+3}	5-4 6-5	2530.49 4658.54	2529.70-2530.83 4657.12-4659.19	4.54 11.62	7-5 8-6	2906.17 4685.22	2905.59-2906.31 4684.31-4685.39	3.59 6.61	3700
C^{+5}	6-5 7-6 8-7	2070.32 3433.69 5290.53	2068.86-2070.87 3431.33-3434.70 5286.99-5292.15	1.94 4.18 9.56	8-6 9-7 10-8 11-9	2082.20 3138.65 4498.79 6200.59	2081.26-2082.34 3137.30-3138.90 4497.01-4499.15 6198.11-6201.20	1.52 3.09 5.73 9.73	3700
O^{+7}	8-7 9-8 10-9	2975.83 4340.58 6068.32	2972.23-2976.34 4335.46-4342.96 6061.33-6071.78	1.92 3.93 7.79	10-8 11-9 12-10 13-11	2530.49 3487.74 4658.53 6064.19	2528.59-2530.85 3485.22-3488.31 4655.27-4659.37 6060.07-6065.38	1.36 2.46 4.25 6.92	3700
N_e^{+9}	9-8 10-9 11-10 12-11	2778.88 3883.63 5249.01 6901.37	2772.73-2780.22 3876.60-3886.87 5239.71-5253.57 6889.37-6907.55	1.30 2.45 4.50 7.97	11-9 12-10 13-11 14-12 15-13	2232.08 2981.38 3881.00 4944.61 6185.87	2229.53-2232.62 2978.09-2982.19 3876.85-3882.16 4939.46-4946.09 6179.58-6187.85	0.823 1.40 2.32 3.72 5.75	3700
A_r^{+17}	13-12 14-13 15-14 16-15 17-16	-2737. -3449. -4276. -5224. -6304.	2721.56-2745.26 3430.30-3460.15 4252.37-4289.35 5196.18-5241.34 6270.13-6324.59		16-14 17-15 18-16 19-17 20-18	-2351. -2857. -3430. -4074. -4795.	2343.51-2353.81 2847.46-2859.95 3418.72-3433.68 4061.50-4079.25 4780.00-4800.87		

Table I Intensity weighted average wavelengths and charge exchange emission measures for visible transitions of hydrogen-like ions. These are obtained for a column emissivity of 1.0×10^{12} photons·cm^{-2}·sec^{-1}, with T_i=Te, N_e=5.0×10^{13} cm^{-3}, $N_i=\frac{1}{2}N_e$, B=0 T, E_H=50 keV/amu.

The effective rate coefficient (cm^{3}·s^{-1}) is obtained immediately as 10^{12}/(emission measure).

TABLE II

Ion	Δn = 1				Δn = 2				T_e
	Trans	Weighted mean wavelength	Component Spread	Emission measure	Trans	Weighted mean wavelength	Component Spread	Emission measure	
		Å	Å	10^{11}cm^{-5}		Å	Å	10^{11}cm^{-5}	eV
O^{+5}	7-6 8-7	3431.14 5287.88	3066.94-3622.53 4749.96-5603.08	3.29 7.05	8-6 9-7 10-8 11-9	2079.68 3135.91 4495.65 6196.96	1932.87-2110.73 2928.31-3191.94 4213.13-4586.81 5823.83-6334.90	11.3 22.0 40.2 68.8	200
N_e^{+7}	8-7 9-8 10-9	2975.47 4340.23 6067.92	2735.58-3107.00 4002.27-4542.63 5608.48-6362.77	1.49 2.88 5.43	10-8 11-9 12-10 13-11	2530.06 3487.25 4657.92 6063.40	2404.26-2567.10 3321.37-3543.97 4444.43-4739.99 5794.15-6177.19	9.93 17.1 28.6 46.4	400
A_r^{+15}	12-11 13-12 14-13 15-14 16-15	-2696. -3464. -4366. -5412. -6612.	2581.74-2769.90 3329.61-3561.54 4186.82-4491.07 5192.61-5569.56 6347.65-6808.07		15-13 16-14 17-15 18-16 19-17 20-18	-2416. -2976 -3616 -4341 -5157 -6069	2357.14-2442.54 2904.60-3009.53 3535.45-3657.82 4240.34-4392.86 5039.12-5220.06 5932.17-6144.88		

Table II Intensity weighted average wavelengths and some charge exchange emission measures for visible transitions of lithium-like ions. These are obtained for a column emissivity of 1.0×10^{12} photons·cm^{-2}·sec^{-1}, with T_i=Te, N_e=5.0×10^{12} cm^{-3}, $N_i = \frac{1}{2} N_e$, B=0 T, E_H=50 keV/amu.

The effective rate coefficient (cm^3·s^{-1}) is obtained immediately as 10^{12}/(emission measure). Note that the component spread is very large in low-Z lithium-like ions. Spectroscopic observations in the wavelength region of peak emission exclude some low ℓ components. The weighted mean wavelength and unresolved emission measure are not directly applicable. The table is relevant to fusion devices of lower central temperature than JET in which the ionisation stage is not edge localised.

TABLE III

Ion	Δn = 1				Δn = 2				T_e
	Trans	Weighted mean wavelength	Component Spread	Emission measure	Trans	Weighted mean wavelength	Component Spread	Emission measure	
		Å	Å	10^{19}cm^{-5}		Å	Å	10^{20}cm^{-5}	eV
A_r^{+7}	8-7 9-8 10-9	2965.13 4330.40 6057.70	2167.93-3619.37 3205.03-5320.73 4527.16-7486.88	1.42 2.71 5.03	10-8 11-9 12-10 13-11	2521.01 3477.87 4647.62 6051.78	2073.97-2686.30 2886.66-3725.28 3885.72-5001.41 5103.96-6538.96	0.910 1.54 2.54 4.05	300
K_r^{+25}	15-14 16-15 17-16 18-17 19-18 20-19	~2049. ~2504. ~3021. ~3605. ~4260. ~4990	1777.47-2221.36 2176.62-2735.65 2631.40-3304.45 3145.43-3946.99 3722.37-4667.77 4365.84-5471.29		20-18	~2298	2114.88-2386.59		

Table III Intensity weighted average wavelengths and some charge exchange emission measures for visible transitions of sodium-like ions. These are obtained for a column emissivity of 1.0×10^{12} photons$\cdot$cm$^{-2}\cdot$sec^{-1}, with T_i=Te, $N_e=5.0\times10^{12}$ cm^{-3}, $N_i=\frac{1}{2}N_e$, B=0 T, E_H=50 keV/amu.

The effective rate coefficient (cm$^3\cdot$s^{-1}) is obtained immediately as 10^{12}/(emission measure).

TABLE IV

Ion		n_{crit}	$N_e = 5.0^{12} cm^{-3}$		$N_e = 1.0^{13} cm^{-3}$		$N_e = 5.0^{13} cm^{-3}$	
	T_e(keV)		n_{ion}	n_{mix}	n_{ion}	n_{mix}	n_{ion}	n_{mix}
H_e^{+2}	3700	2	12	4	10	4	8	3
B_e^{+4}	3700	3	20	6	18	6	15	5
C^{+6}	3700	4	>20	8	>20	8	20	7
O^{+8}	3700	5	>20	10	>20	9	>20	8
N_e^{+10}	3700	6	>20	12	>20	11	>20	9

Table IV Critical parameters of main impurity ion for JET related conditions.

TABLE V

Author		Approximation	Recombining Ion	n-range	Energy range keV/amu
Ryufuku (1982)	29-31	UDWA	He^{+2}	1-5	10-200
Rapp (1974)	32	CCAO	"	1-4	0.1-75
Ryufuku (1982)	29-31	UDWA	C^{+6}	1-8	10-200
Fritsch (1984) Fritsch & Lin (1984)	33 34	CCAO	"	4-8	0.1-30
Olsen (1981)	35,36	CTMC	"	4-8	50-100
Green et al (1982)	37	CCMO	"	3-5	1.31-34.02
Ryufuku (1982)	29-31	UDWA	O^{+8}	2-10	10-200
Fritsch (1984) Fritsch & Lin (1984)	33 34	CCAO	"	4-10	0.1-30
Olsen (1981)	35,36	CTMC	"	4-10	50-100
Shipsey et al (1983)	38	CCMO	"	4-7	1.31-34.02

Table V Sources for primary charge exchange capture cross-sections. Use of a particular approximation means use of that approximation within its defined energy range, but extended to higher energy by UDWA and to lower energy by CCAO. UDWA data is used for all other recombining ions by interpolation in nuclear charge if necessary. Non-hydrogenic ions are treated as the hydrogenic ion of the same ion charge with capture to lowest closed shells excluded.

TABLE VI

No.	Form	Parameters
1	$N(2\ell+1)e^{-\ell/\ell_{cut}} \quad \ell\leq n-1$	ℓ_{cut}
2	$\begin{cases} N(2\ell+1) & \ell\leq\ell_{cut} \\ 0 & \ell_{cut}<\ell\leq n-1 \end{cases}$	ℓ_{cut}
3	$\begin{cases} N(2\ell+1)^2 & \ell\leq\ell_{cut} \\ 0 & \ell_{cut}<\ell\leq n-1 \end{cases}$	ℓ_{cut}
4	$\delta(\ell,\ell_{cut} \quad \ell\leq n-1$	ℓ_{cut}
5	$N(2\ell+1)e^{-max(o,\ell-\ell_{cut})/2} \quad \ell\leq n-1$	ℓ_{cut}
6	$N(2\ell+1)e^{-2xmax(o,\ell-\ell_{cut})} \quad \ell\leq n-1$	ℓ_{cut}

Table VI Algebraic forms used for ℓ distributions of primary charge exchange capture with form factor ℓ_{cut}. The parameter N normalises the sum over ℓ to unity.

Table VII

	carbon		oxygen
	$\frac{q^{CEM}(10\rightarrow8)}{q^{CEM}(8\rightarrow7)}$	$\frac{q^{CEM}(11\rightarrow9) + q^{CEM}(13\rightarrow10)}{q^{CEM}(8\rightarrow7)}$	$\frac{q^{CEM}(10\rightarrow9)}{q^{CEM}(9\rightarrow8)}$
experimental	0.15	0.10	0.42
Ryufuku[26-28]	0.11	0.07	0.45
Fritsch and Lin[30,31]	0.13	0.09	0.55
Olson[32,33]	0.11	0.07	0.35
Shipsey et al[34,35]	0.144	0.10	0.38

Table VII Comparison of experimental and theoretical ratios of carbon charge exchange rate coefficients. These ratios are quite insensitive to plasma parameters.

TABLE VIII

	primary CX rates (cm^3/sec)	
	experimental	theory
n=8	1.79×10^{-8}	2.02×10^{-8}
n=9	1.09×10^{-8}	1.01×10^{-8}
n=10	6.88×10^{-9}	5.41×10^{-9}
n dependence	~ $n^{-2.5}$	n^{-3}

Table VIII Comparison of experimental and theoretical primary charge exchange rate coefficients into quantum shells 8 and 10.

TABLE IX

r	T_e	N_e	$N(H(1s))$	$\frac{N(H(n=2))}{N(H(1s))}$	$N(C^{+6})$	$q^{CEM}_{H(n=2)}$	I	$N(O^{+6})$	$q^{CEM}_{H(n=2)}$	I	$N(C^{+5})$	q^{EEM}	I	$N(O^{+5})$	q^{EEM}	I
cm	eV	10^{12} cm^{-3}	10^{9} cm^{-3}	10^{-4}	10^{11} cm^{-3}	10^{-8} cm^{3} s^{-1}	10^{9} cm^{-2} s^{-1}	10^{9} cm^{-3}	10^{-8} cm^{3} s^{-1}	10^{9} cm^{-2} s^{-1}	10^{9} cm^{-3} s^{-1}	10^{-14} cm s^{-1}	10^{9} cm^{-2} s^{-1}	10^{9} cm^{-3}	10^{-12} cm s^{-1}	10^{9} cm^{-2} s^{-1}
81.0	1671	10.7			3.35			0.07			0.34	12.0	2.29			
85.7	1477	9.25			3.16			0.32			0.91	12.0	4.37			
89.7	1301	7.96			3.00			1.10			2.73	12.0	9.78			
93.2	1131	8.61	0.36	3.73	2.81	12.0	15.1	2.91			7.16	11.5	18.5			
96.3	965	5.77	0.55	3.28	2.60	11.7	16.5	6.33			15.3	10.8	28.6			
99.2	803	4.83	0.87	2.87	2.33	11.4	18.6	11.7	12.1	0.99	27.2	10.1	37.2	0.11	6.45	9.86
101.9	649	3.98	1.32	2.48	2.00	11.1	18.5	18.6	11.8	1.83	39.7	8.90	35.9	0.64	6.45	41.8
104.3	508	3.21	1.96	2.12	1.65	10.8	17.4	25.3	11.5	2.84	48.2	7.74	28.1	2.41	6.39	116
106.6	384	2.53	2.75	1.75	1.28	10.5	14.6	28.7	11.3	3.51	48.8	5.90	16.4	5.91	6.32	213
108.8	280	1.92	2.63	1.42	0.92	10.2	10.2	22.9	11.0	2.73	40.5	4.10	6.70	9.28	6.25	234
110.8	195	1.42	4.79	1.07	0.59	9.99	5.9	13.7	10.7	1.47	27.6	3.00	2.29	9.24	6.18	158
112.7	101	0.90	6.03	0.68	0.30	9.96	2.3	6.90	10.7	0.56	14.2			5.49	6.00	56.1
114.6	37.5	0.43	7.59	0.28	0.14	9.93	0.4	3.27	10.1	0.13	6.72			2.64	6.00	12.4
116.3	16.6	0.22			0.07			1.59			3.26			1.29	6.00	2.87
					Sum (x2)*		240	Sum (x2)*		28.1	Sum (x2)*		38.0	Sum (x2)*		1690

* to account for both edges

Table IX Analysis of apparent C^{+5} (8→7) cold feature. Theoretical contributions to observed column emissivity $4.0\times10^{12}\cdot\mathrm{cm}^{-2}\cdot\mathrm{sec}^{-1}\cdot\mathrm{sr}^{-1}$ are listed for $\frac{N_C}{N_e} \simeq 3.1\%$, $\frac{N_O}{N_e} \simeq 1.0\%$ and $Z_{eff} \simeq 2.5$.

TABLE X

Energy keV/amu	C-VI 8→7 10^{-9} cm$^3\cdot$s^{-1}	O-VIII 9→8 10^{-8} cm$^3\cdot$s^{-1}	O-VIII 10→9 10^{-9} cm$^3\cdot$s^{-1}	He-I 4→3 10^{-9} cm$^3\cdot$s^{-1}
11	0.10	0.02	0.06	0.27
12	0.20	0.05	0.12	0.40
13	0.31	0.07	0.18	0.53
14	0.43	0.10	0.26	0.67
15	0.55	0.13	0.34	0.82
16	0.69	0.16	0.42	0.98
17	0.83	0.19	0.51	1.1
18	0.99	0.23	0.61	1.3
19	1.2	0.26	0.72	1.5
20	1.3	0.30	0.83	1.7
22	1.7	0.39	1.1	2.1
24	2.2	0.48	1.4	2.5
26	2.7	0.60	1.9	2.8
28	3.2	0.74	2.6	2.9
30	3.7	0.90	3.4	3.0
32	4.3	1.1	4.2	3.1
34	5.0	1.2	5.1	3.2
36	5.7	1.4	6.0	3.3
38	6.4	1.6	7.0	3.4
40	7.1	1.8	8.1	3.4
42	8.0	2.1	9.3	3.5
44	8.8	2.3	11	3.6
46	9.8	2.5	12	3.7
48	11	2.7	13	3.8
50	12	3.0	15	3.9
60	12	2.9	15	3.3
70	11	2.8	15	2.6
80	11	2.5	15	2.1
90	9.5	2.2	13	1.7
100	8.1	1.9	11	1.3

Table X Charge exchange rate coefficients as a function of neutral particle energy assuming an effective ion density of 1.5×10^{13}cm^{-3}, an ion temperature of 6 keV and an effective ion charge of 2.

TABLE XI

Ion Density	C-VI 8→7	O-VIII 9→8	O-VIII 10→9	He-I 4→3
10^{19} m^{-3}	10^{-9} cm$^3\cdot$s^{-1}	10^{-8} cm$^3\cdot$s^{-1}	10^{-9} cm$^3\cdot$s^{-1}	10^{-9} cm$^3\cdot$s^{-1}
0.02	7.3	1.8	8.5	4.4
0.1	7.2	1.8	8.4	4.0
0.5	6.8	1.6	7.6	3.5
1.0	6.3	1.5	7.0	3.4
2.0	5.8	1.4	6.1	3.3
3.0	5.4	1.3	5.6	3.2
5.0	4.9	1.1	5.0	3.2
7.0	4.7	1.0	4.6	3.2

Table XI Charge exchange rate coefficients as a function of the effective ion density at fixed energy (37 keV/amu), assuming Z_{eff}=2, T_i=6 keV and n_i=1.5x10^{13} cm^{-3}.

TABLE XII

T_i	C-VI 8→7	O-VIII 9→8	O-VIII 10→9	He-I 4→3
keV	10^{-9} cm$^3\cdot$s^{-1}	10^{-8} cm$^3\cdot$s^{-1}	10^{-9} cm$^3\cdot$s^{-1}	10^{-9} cm$^3\cdot$s^{-1}
1.0	5.8	1.4	5.7	3.2
4.0	6.2	1.5	6.3	3.3
8.0	6.4	1.5	6.6	3.3
14.0	6.5	1.6	6.9	3.4
24.0	6.7	1.6	7.1	3.4

Table XII Charge exchange rate coefficients as a function of the ion temperature, assuming E_o=37 keV/amu, Z_{eff}=2 and n_i=1.5x10^{13} cm^{-3} (except for C VI 8-7 where n_i=1.0x10^{13} cm^{-3}).

TABLE XIII

Z_{eff}	C-VI 8→7	O-VIII 9→8	O-VIII 10→9	He-I 4→3
10^{19} m^{-3}	10^{-9} cm$^3\cdot$s^{-1}	10^{-8} cm$^3\cdot$s^{-1}	10^{-9} cm$^3\cdot$s^{-1}	10^{-9} cm$^3\cdot$s^{-1}
1.0	6.9	17	7.7	3.6
2.0	6.0	14	6.5	3.3
3.0	5.3	13	5.6	3.2
4.0	4.9	11	4.9	3.2
5.0	4.6	10	4.4	3.2
6.0	4.3	9.2	4.1	3.2

Table XIII Charge exchange rate coefficients as a function of the effective ion charge, assuming E_o=37 keV/amu, T_i=6 keV and n_i=1.5x10^{13} cm^{-3}.

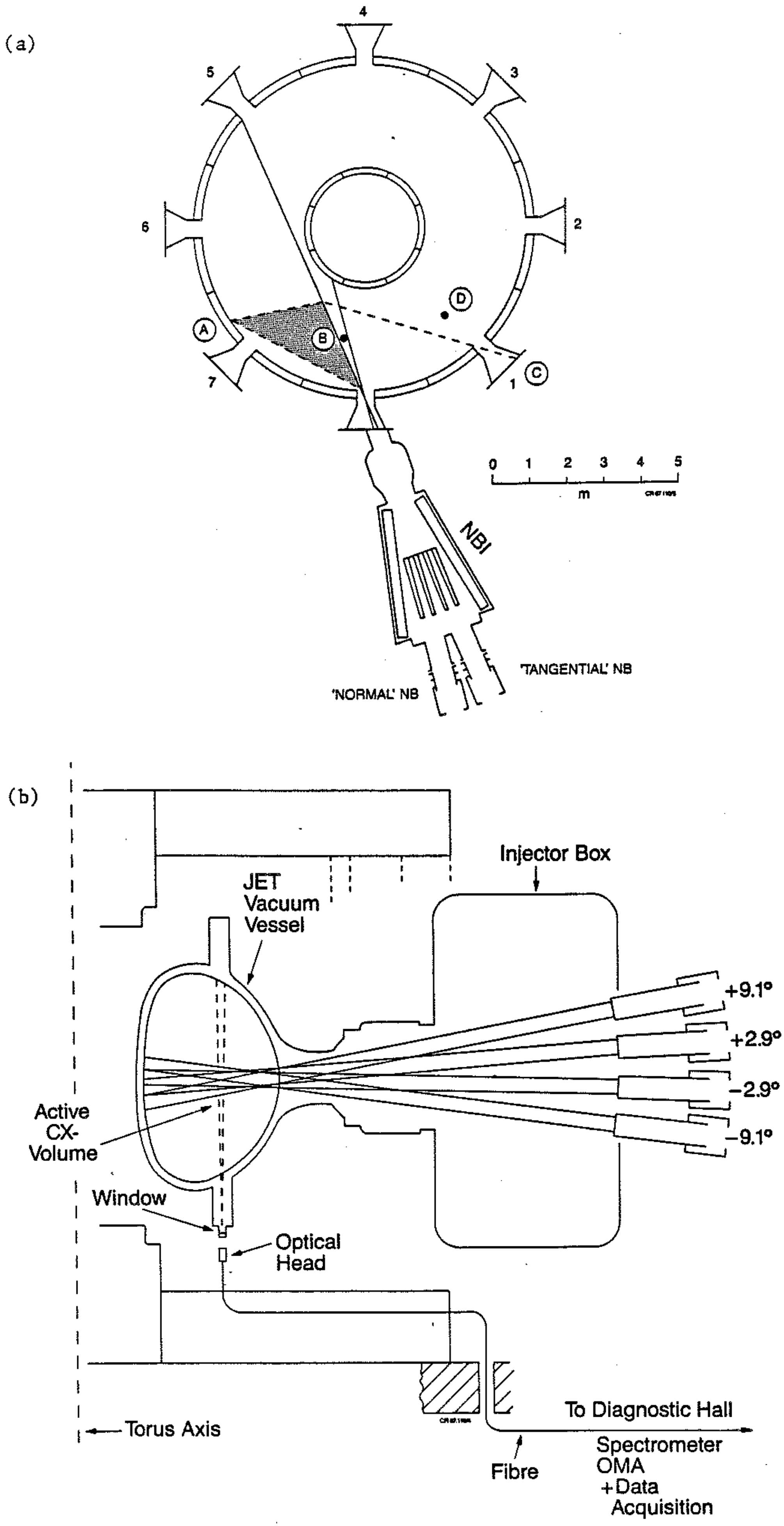

Fig.1 Schematic views of JET showing the lines of sight of the CXRS diagnostic and the heating neutral beams.

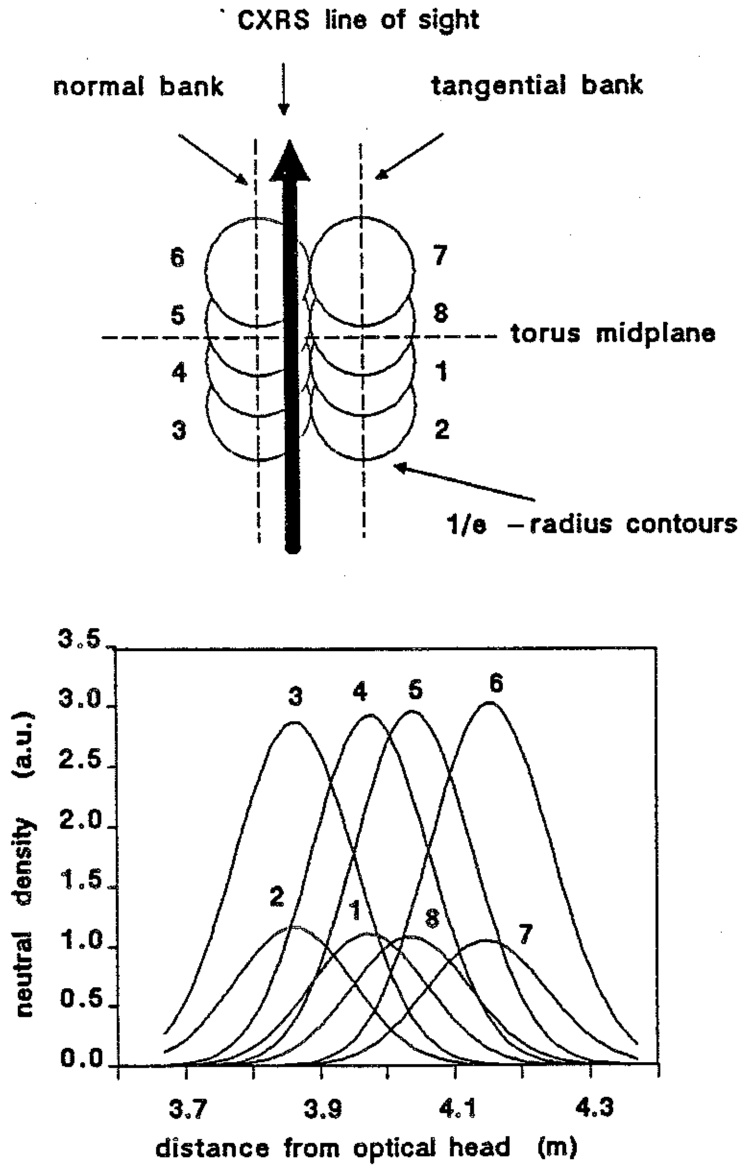

Fig.2 Contribution of normal and tangential beams to the vertical line of sight. The calculated neutral particle density reflects the slightly tilted viewing line.

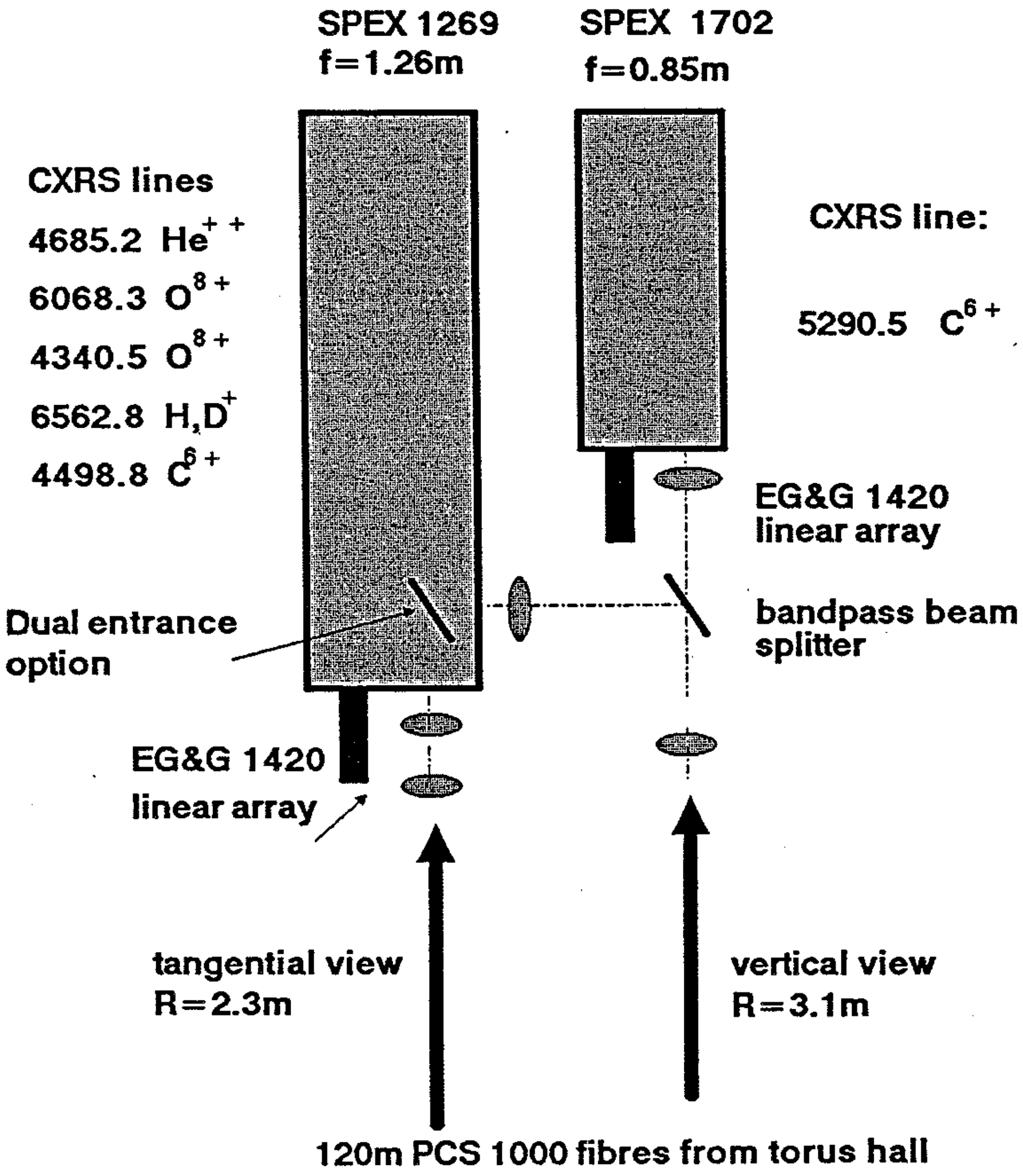

Fig.3 Dual spectrometer layout.

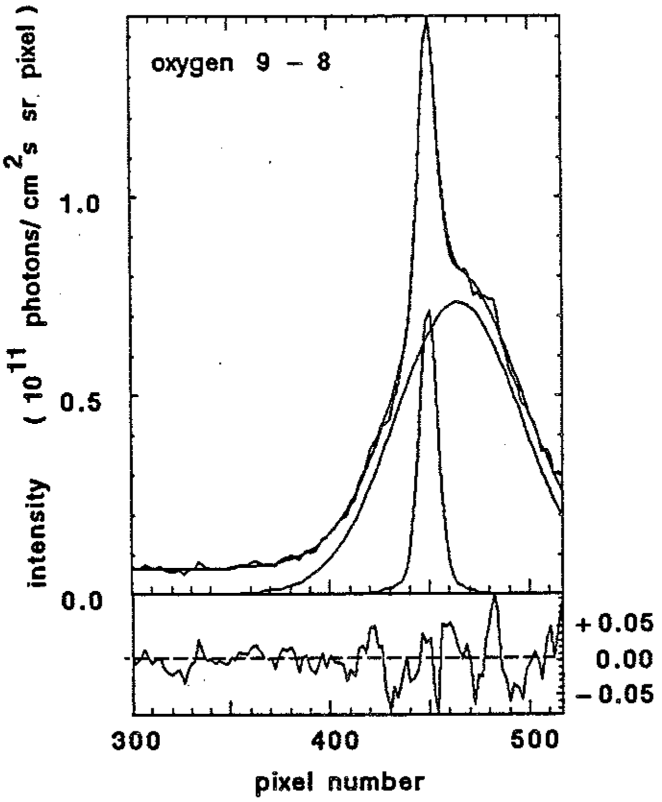

Fig.4 Spectral line profile of the oxygen n=9 to n=8 transition near 4340.5 Å (T_{cx}=5.7 keV ± 0.2 keV). The narrow line corresponds to the D_γ transitions. (JET pulse 10645; dispersion : 0.0840 Å/pixel).

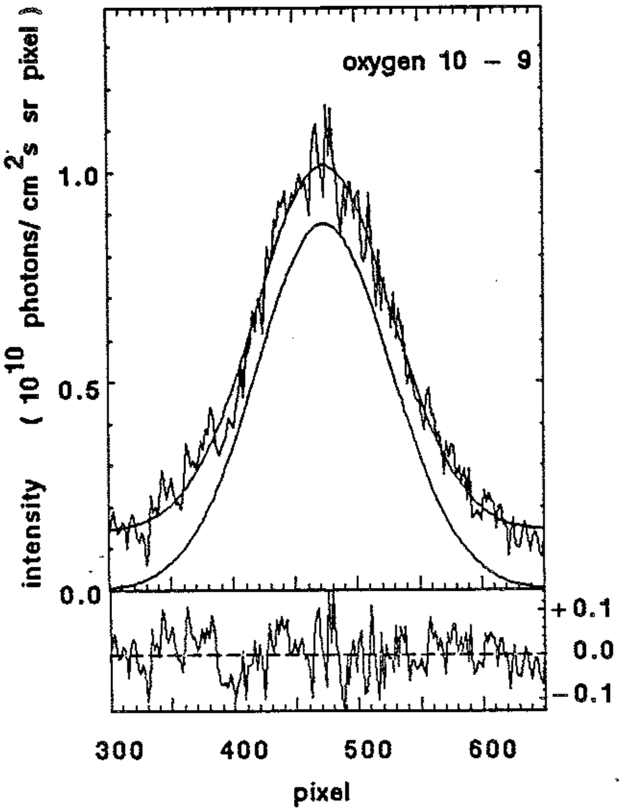

Fig.5 Spectral line profile of the oxygen n=10 to n=9 transition near 6068.3 Å (T_{cx}=5.7 keV ± 0.2 keV). (JET pulse 10644; dispersion : 0.0717 Å/pixel).

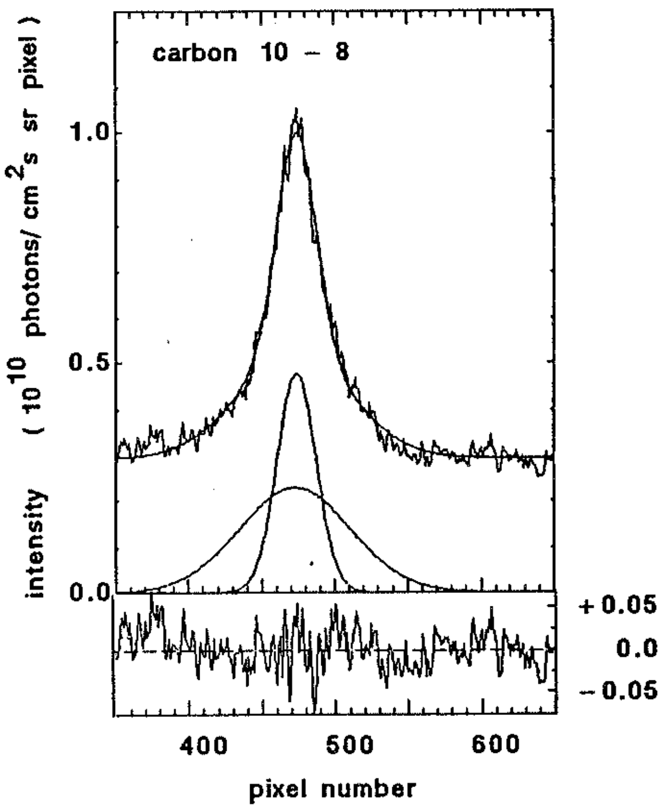

Fig.7 Spectral line profile of the carbon n=10 to n=8 transition near 4498.8 A (T_{cx}=5.0 keV ± 0.4 keV). A cold component is also superimposed onto the charge exchange signal.(JET pulse 10948; dispersion : 0.0831 A/pixel).

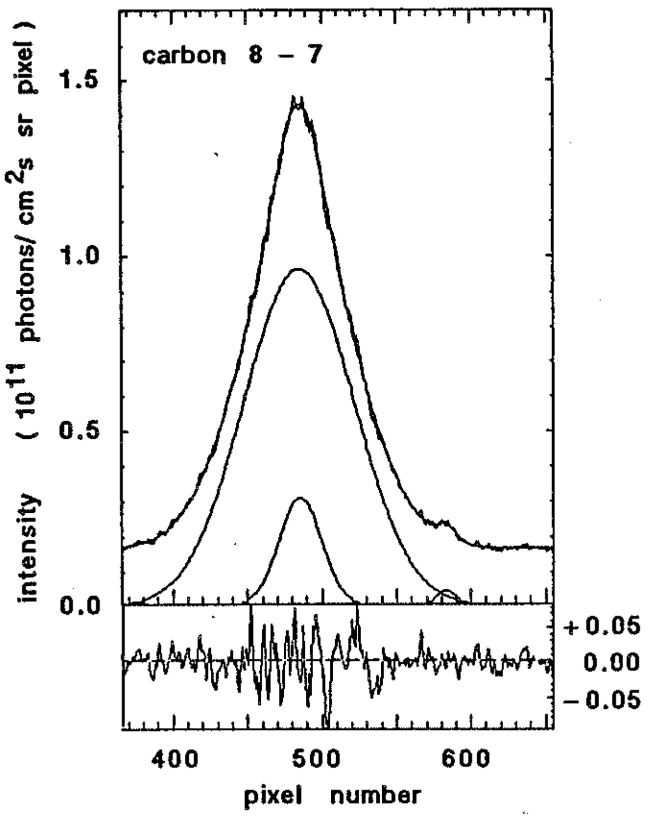

Fig.6 Spectral line profile of the carbon n=8 to n=9 transition near 5290.5 A (T_{cx}=10.2 keV ± 0.2 keV). It also shows the cold feature observed on carbon spectra at the same wavelengths as the charge exchange signal. The small satellite on the right wing is an O IV transition near 5305.3 A.(JET pulse 10143; dispersion : 0.0410 A/pixel).

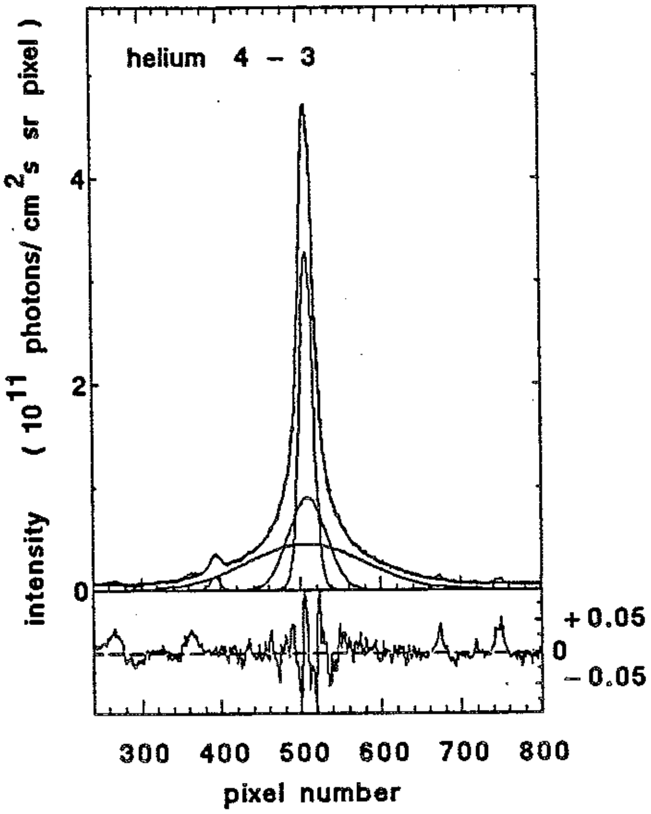

Fig.8 Spectral line profile of the helium n=4 to n=3 transition near 4685.2 A (T_{cx}=7.2 keV ± 0.5 keV). The cold feature must be represented by 2 narrow Gaussians, as can also be observed without neutral beam injection. (JET pulse 10205; dispersion : 0.1640 A/pixel).

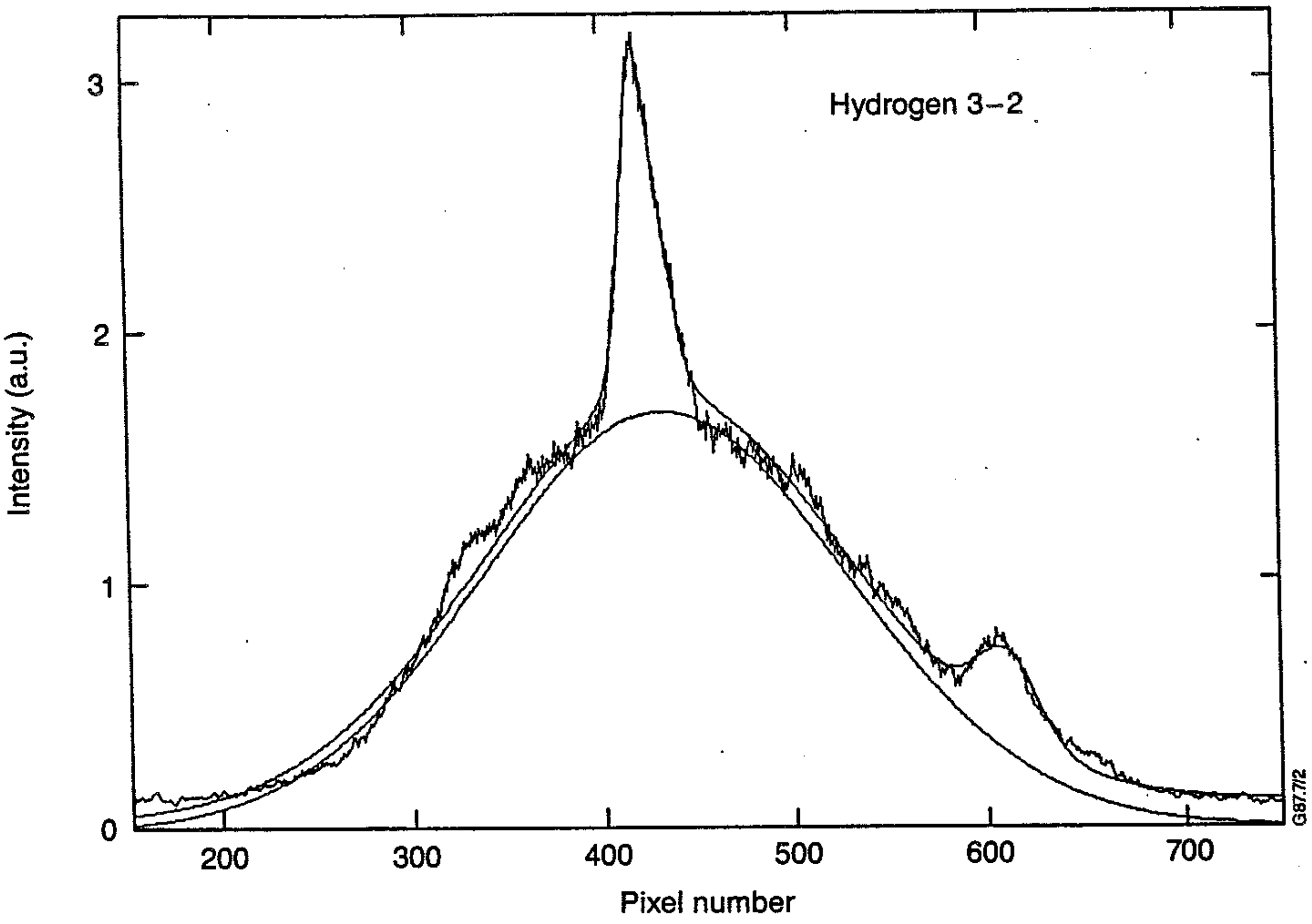

Fig.9 spectral line profile of the hydrogen n=3 to n=2 transition near 6562.8 A. (JET pulse 7145; dispersion : 0.133 A/pixel).

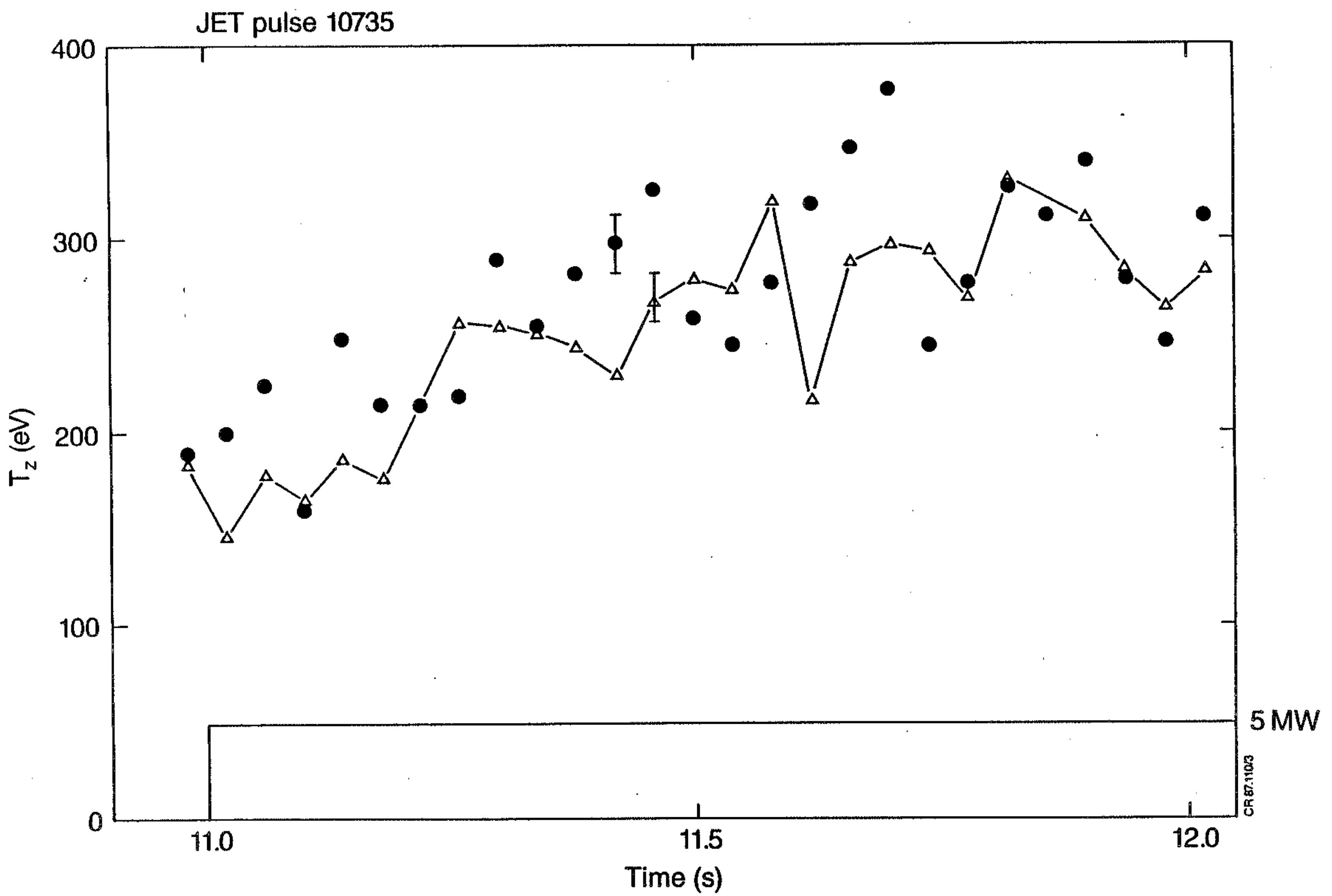

Fig.10 Evolution of the carbon 5290.5 Å cold component temperature as measured with the passive (triangles) and active (circles) lines of sight.

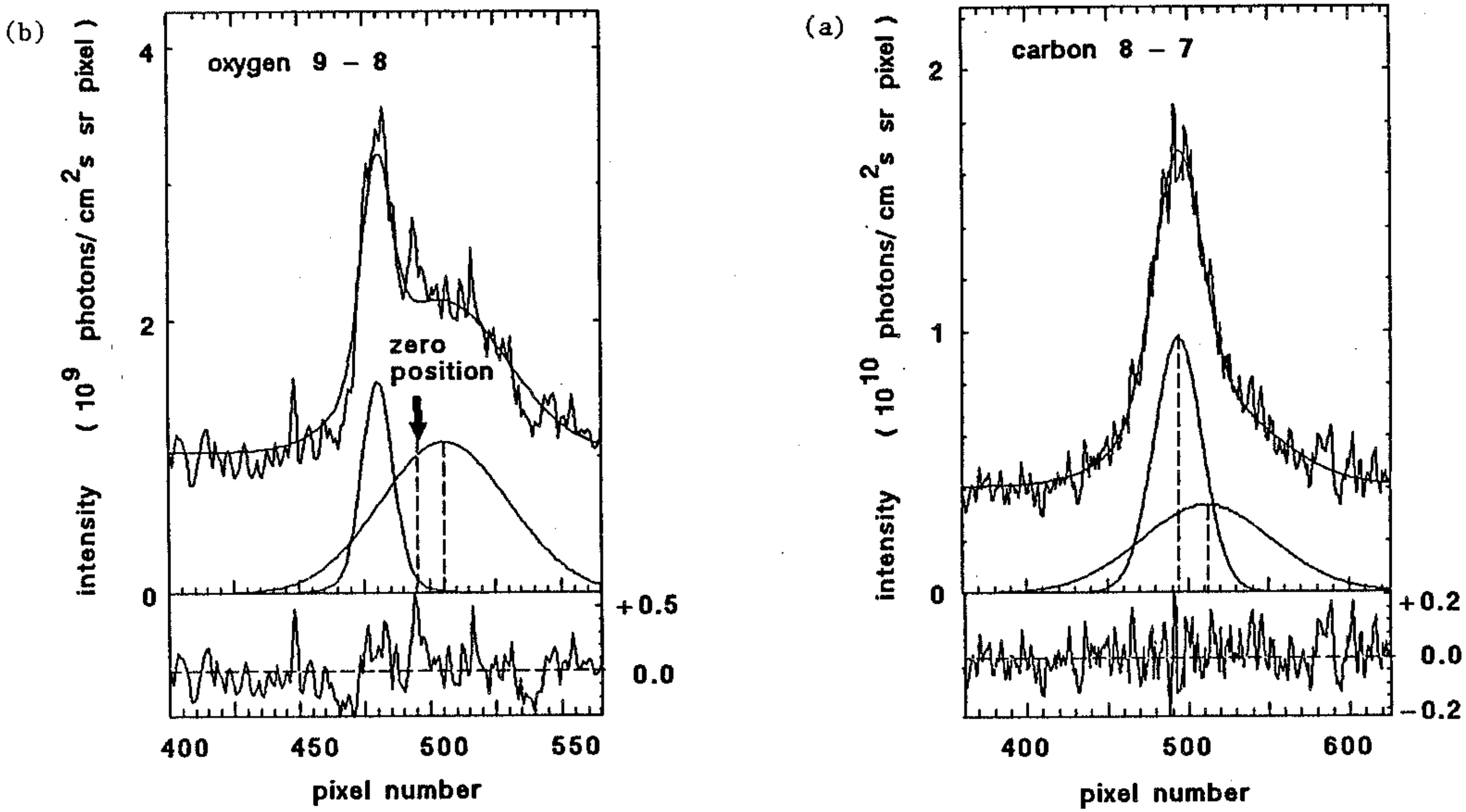

Fig.11 Spectral line profiles measured with the horizontal line of sight (active volume near r/a ~ 0.65 on the high field side). The dashed line indicates the position of the unshifted cx line. (a) Carbon 5290.5 Å transition; JET pulse 10745 ($T_{cx} \sim 4.1$ keV ± 0.5 keV, $v_{rot} \sim 8.4 \times 10^4$ m/s ± 1.0×10^4 m/s), (b) oxygen 4340.5 Å transition; JET pulse 10740 ($T_{cx} \sim 3.0$ keV ± 0.3 keV, $v_{rot} \sim 6.7 \times 10^4$ m/s ± 0.7×10^4 m/s).

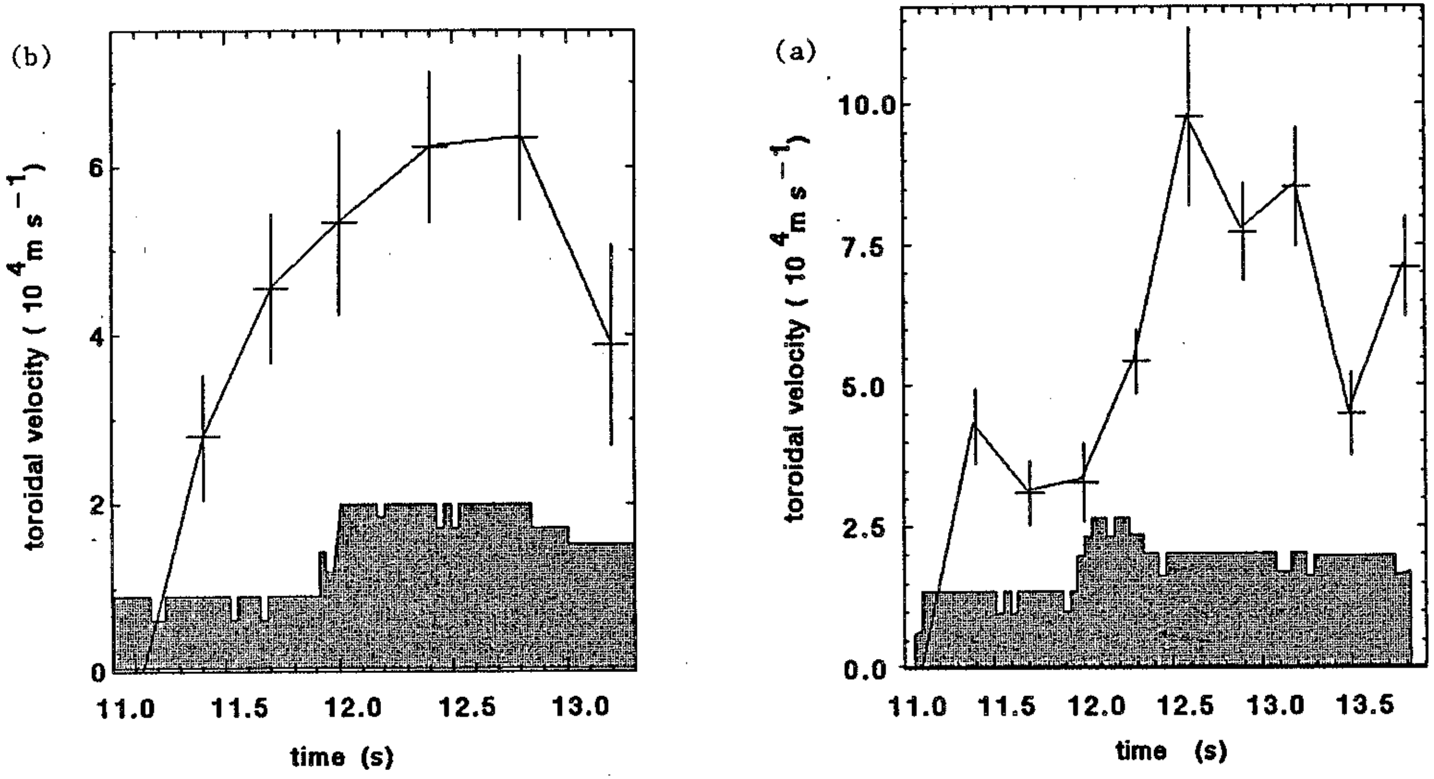

Fig.12 Toroidal rotation velocity measurement on the high field side near $r/a \sim 0.65$ showing a delay of a few hundred ms before saturation at fixed beam power. (a) From the C VI 5290.5 Å transition; JET pulse 10745 (b) from the O VIII 4340.5 Å transition; JET pulse 10740.

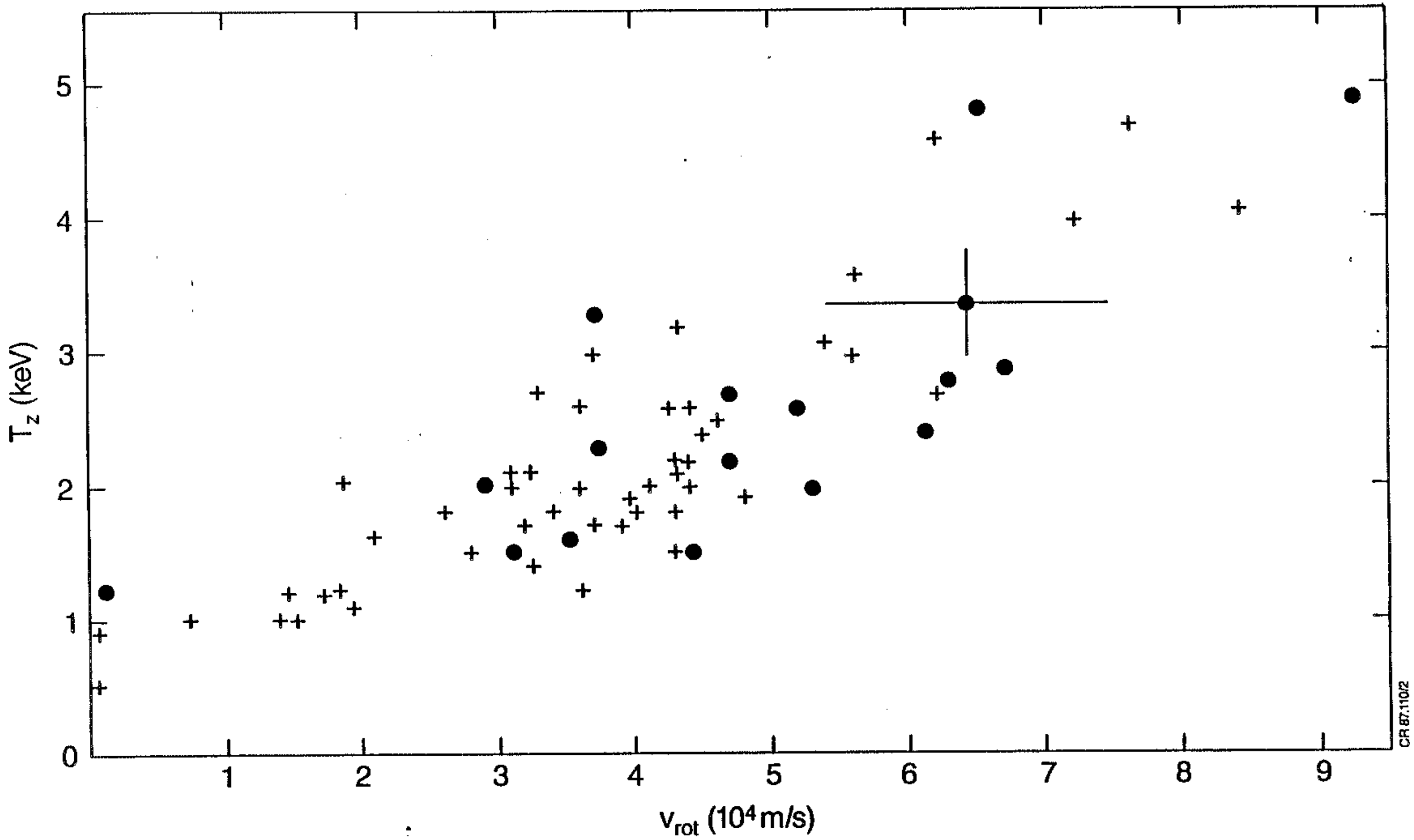

Fig.13 Scaling of local impurity ion temperature and toroidal rotation velocity measured by CXRS near r/a - 0.65 on the high field side. Transient points when the neutral beam power is stopped are also included (o C VI 5290.5 Å line; + O VIII 4340.5 Å line).

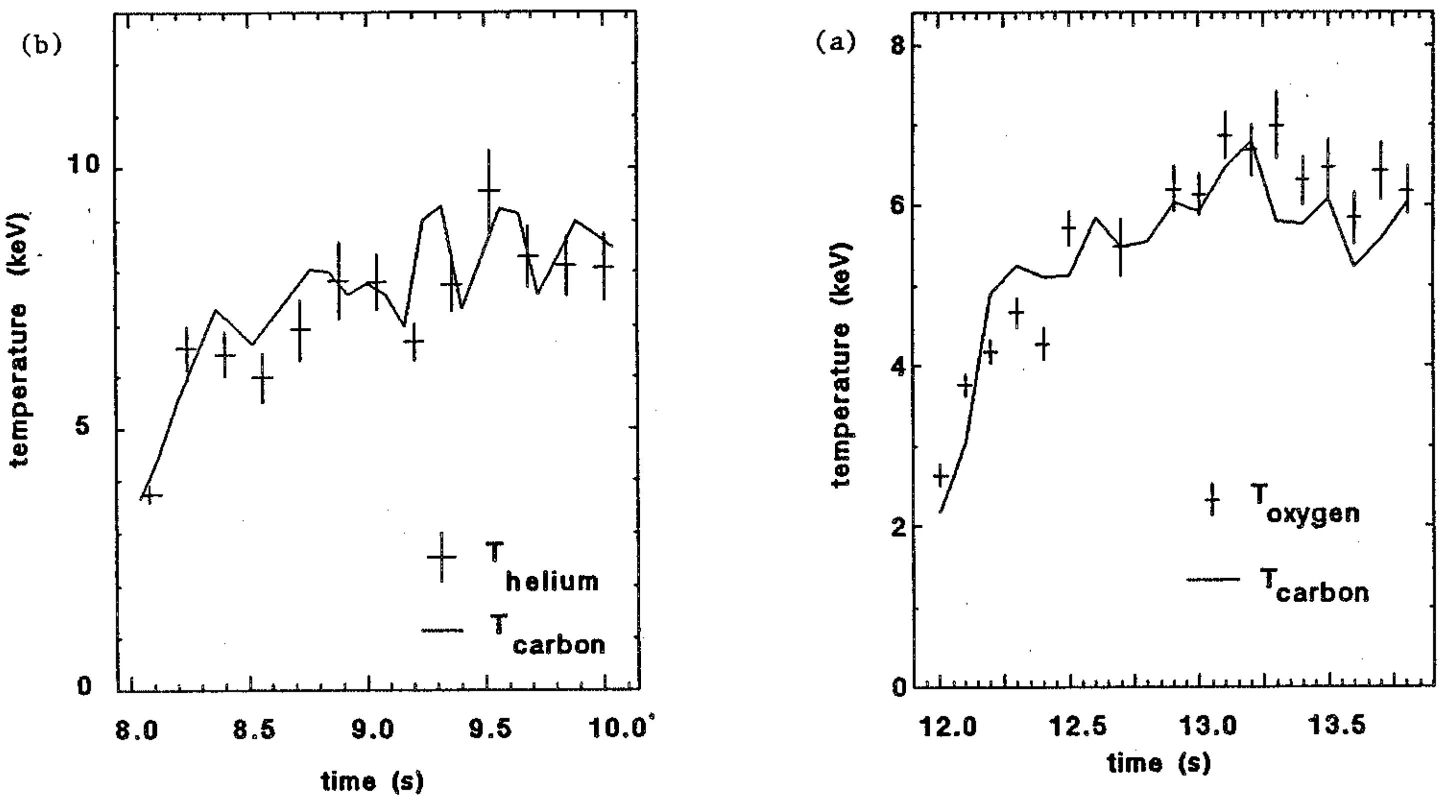

Fig.14 Comparison of light impurities temperature showing no mass dependence. (a) Carbon 5290.5 Å and Helium 4685.2 Å (dotted line) JET pulse 10145; (b) carbon 5290.5 Å and oxygen 4340.5 Å (dotted line), JET pulse.

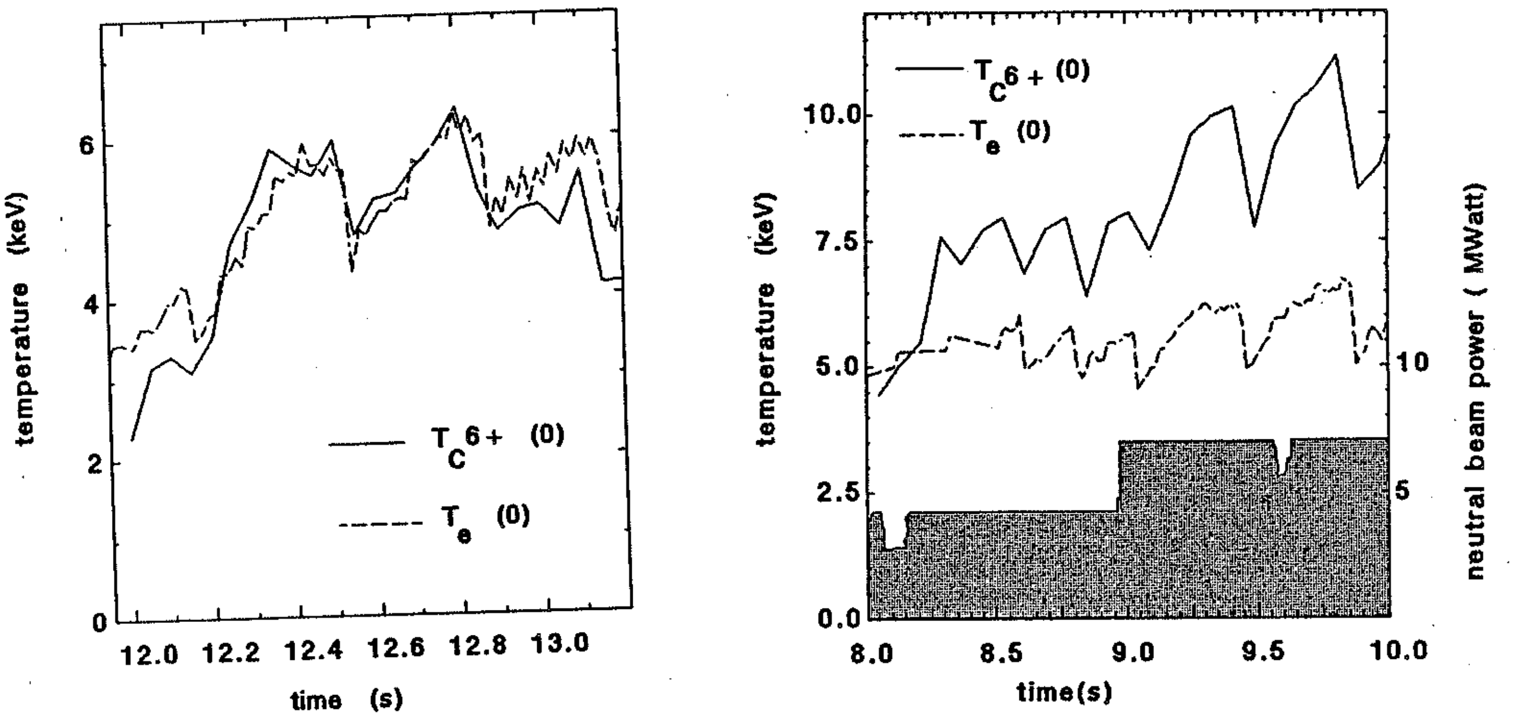

Fig.15 Comparison between the impurity ion (carbon 5290.5 Å) and electron (dotted line) temperatures on axis for different additional heating schemes. (a) Low density, inner wall plasma JET pulse 10143; (b) high density, X-point plasma, JET pulse 10645.

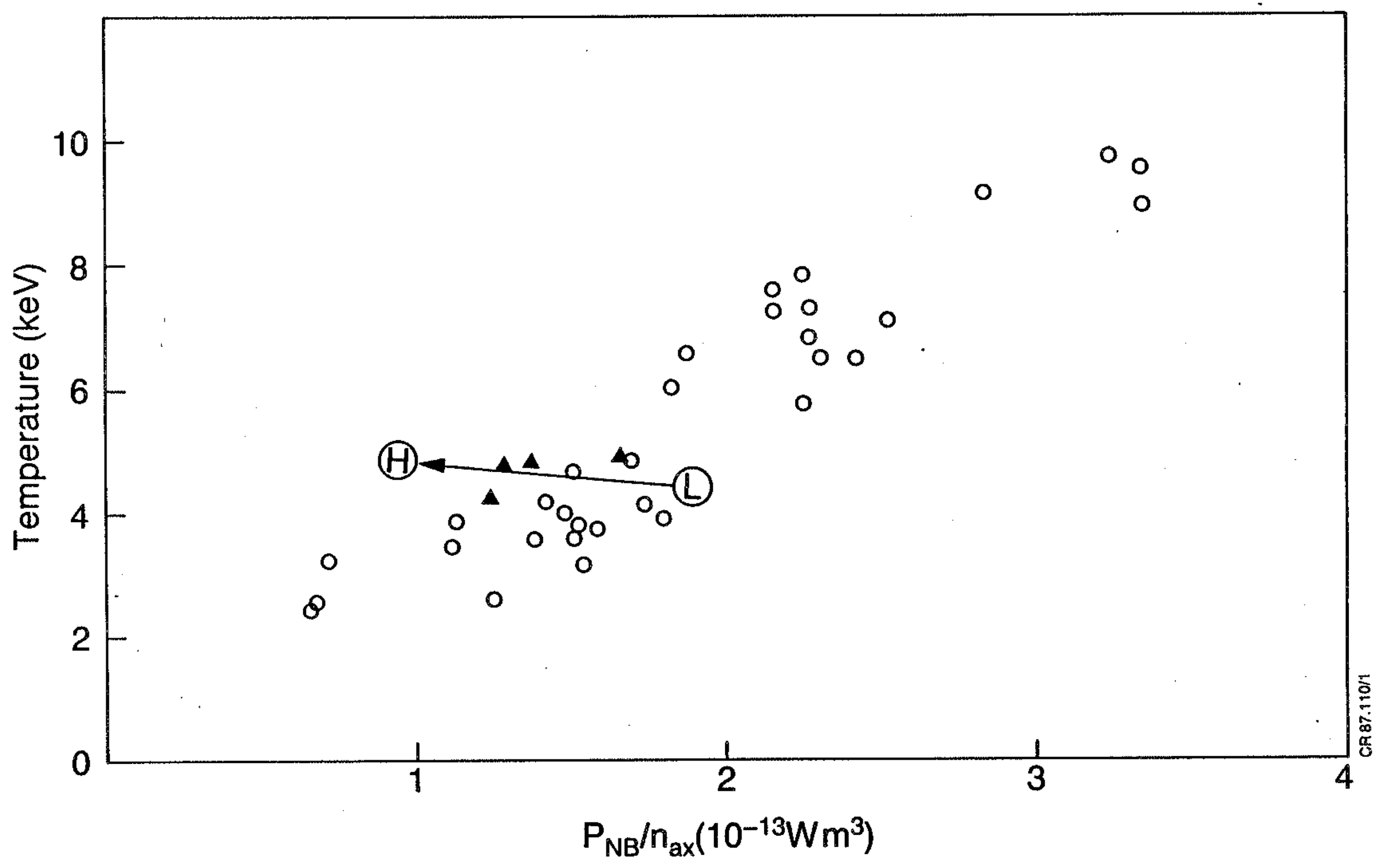

Fig.16 Scaling of the central impurity ion temperature with the neutral beam power normalized to the electron density on axis (+ inner wall, I_p=3 MA; o inner wall, I_p=5 MA; L : x-point, L-mode; H : X-point, H-mode).

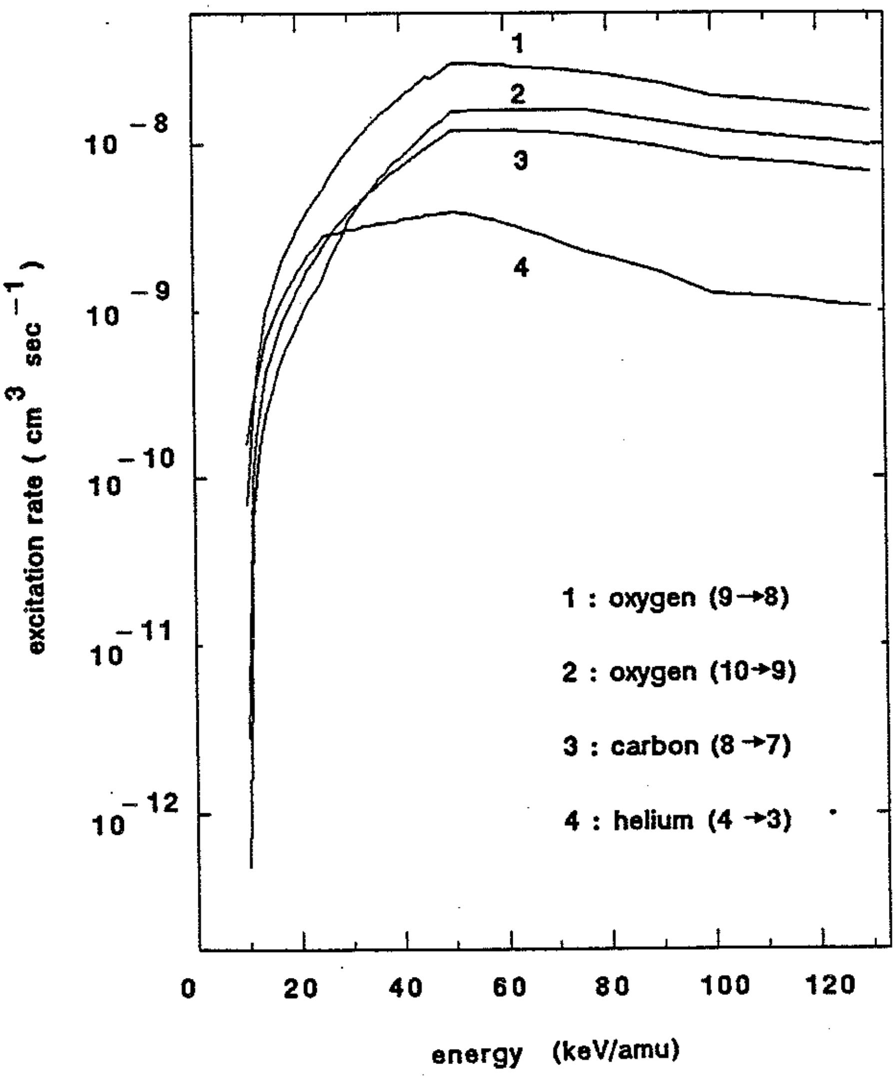

Fig.17 Variation of effective charge exchange rate coefficients with hydrogen neutral beam energy (nℓ-picture).

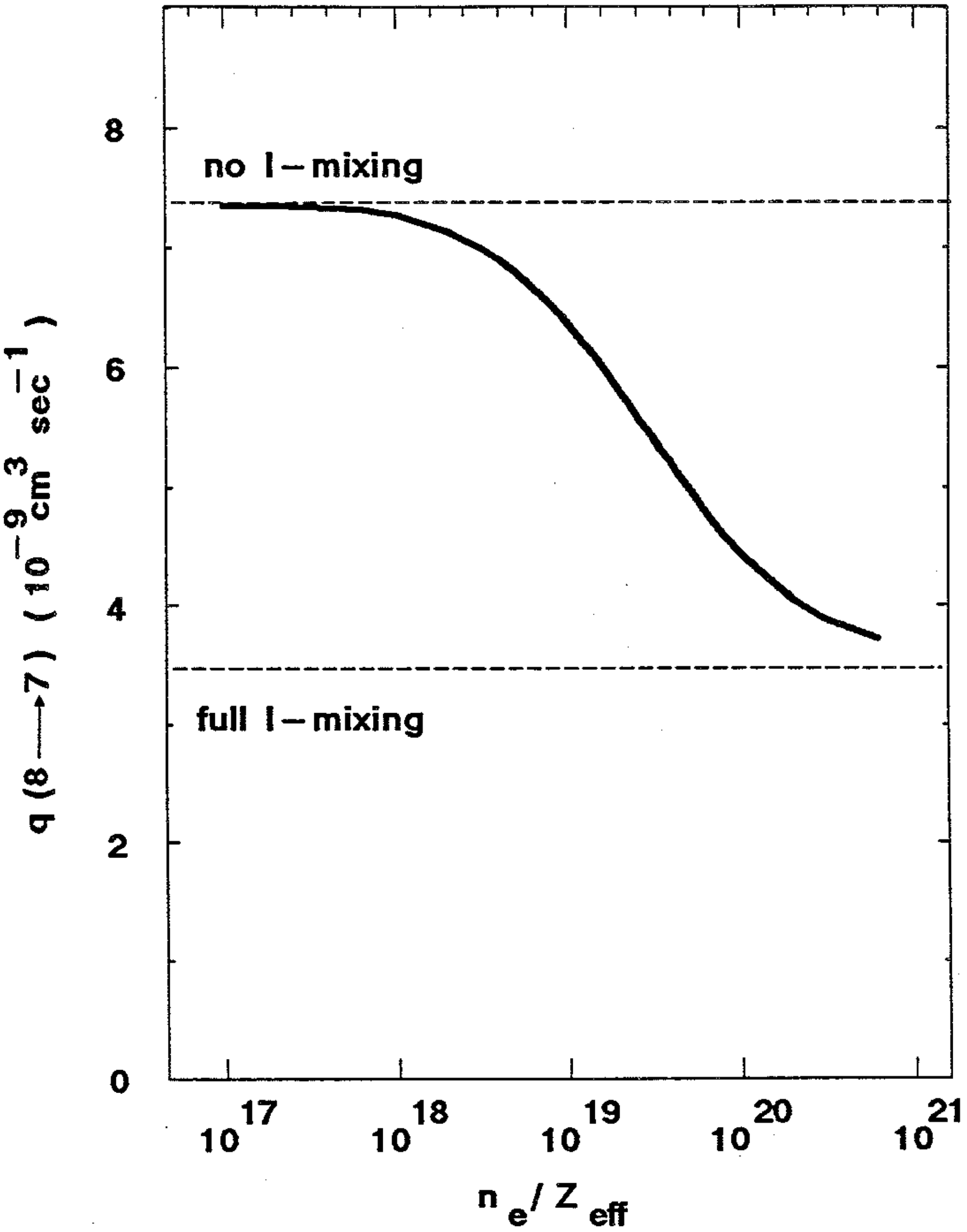

Fig.18 Influence of ℓ-mixing on C VI 8→7 effective charge exchange rate coefficients (nℓ-picture). The values for no ℓ-mixing and full ℓ-mixing are taken from Ref.25.

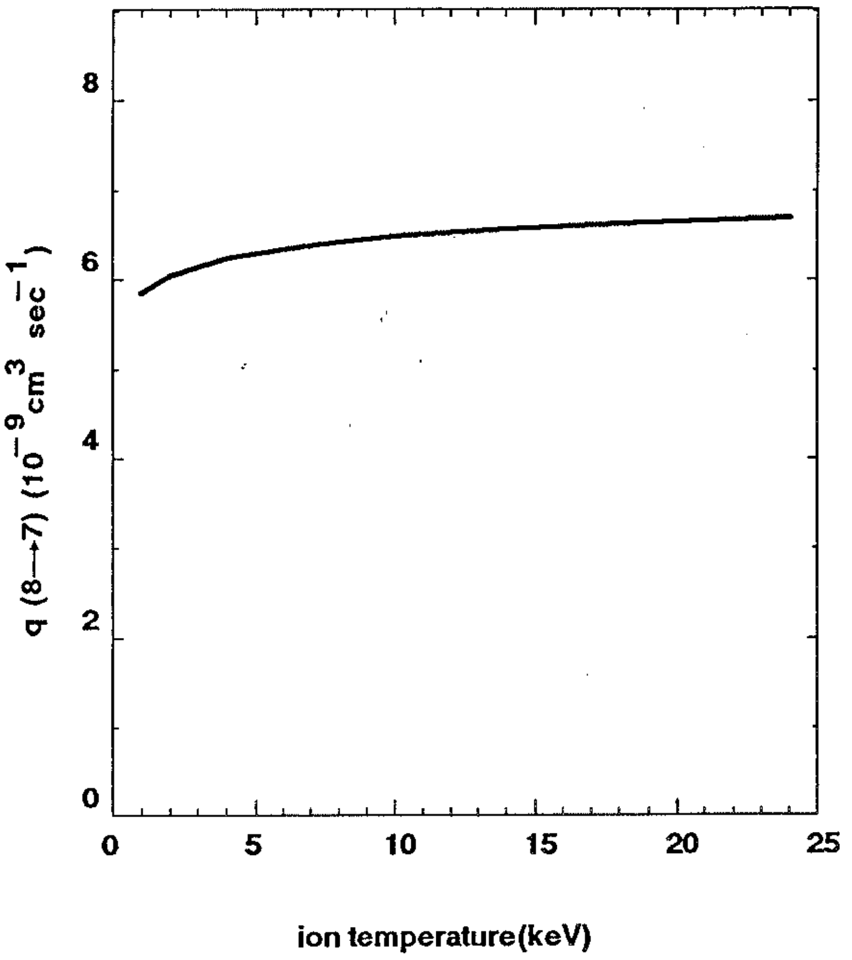

Fig.20 Influence of background (Z_{eff}) ion temperature on C VI 8→7 effective charge exchange rate coefficients (nℓ-picture).

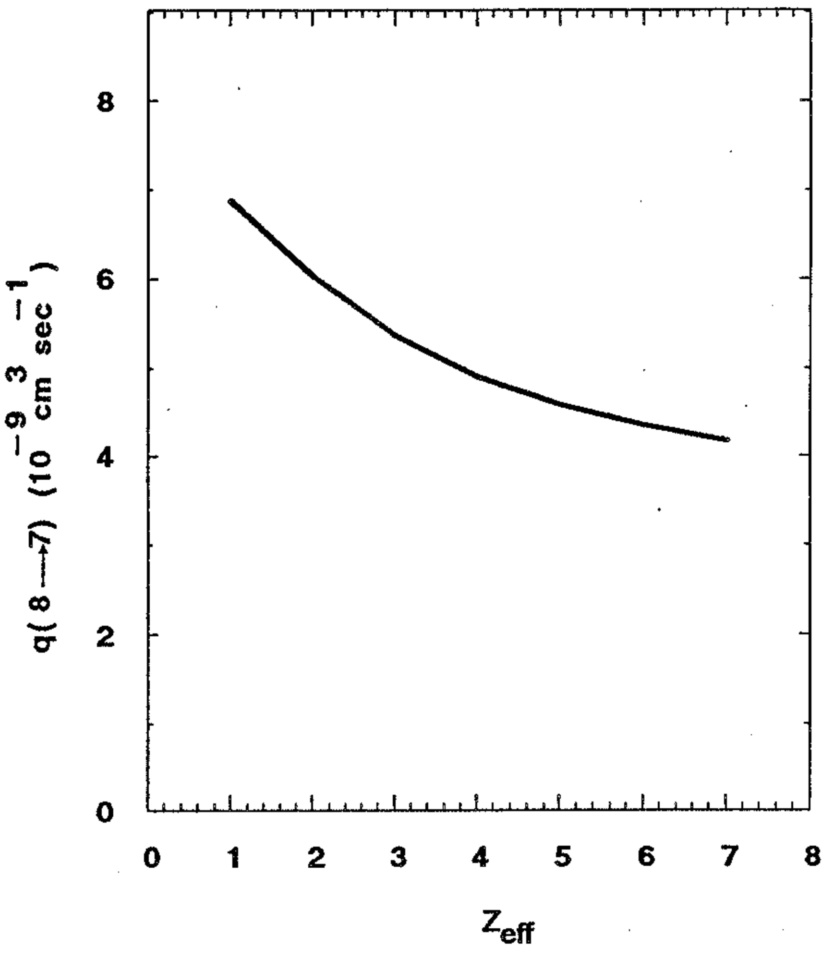

Fig.19 Influence of Z_{eff} background ions on C VI 8→7 effective charge exchange rate coefficients (nℓ-picture).

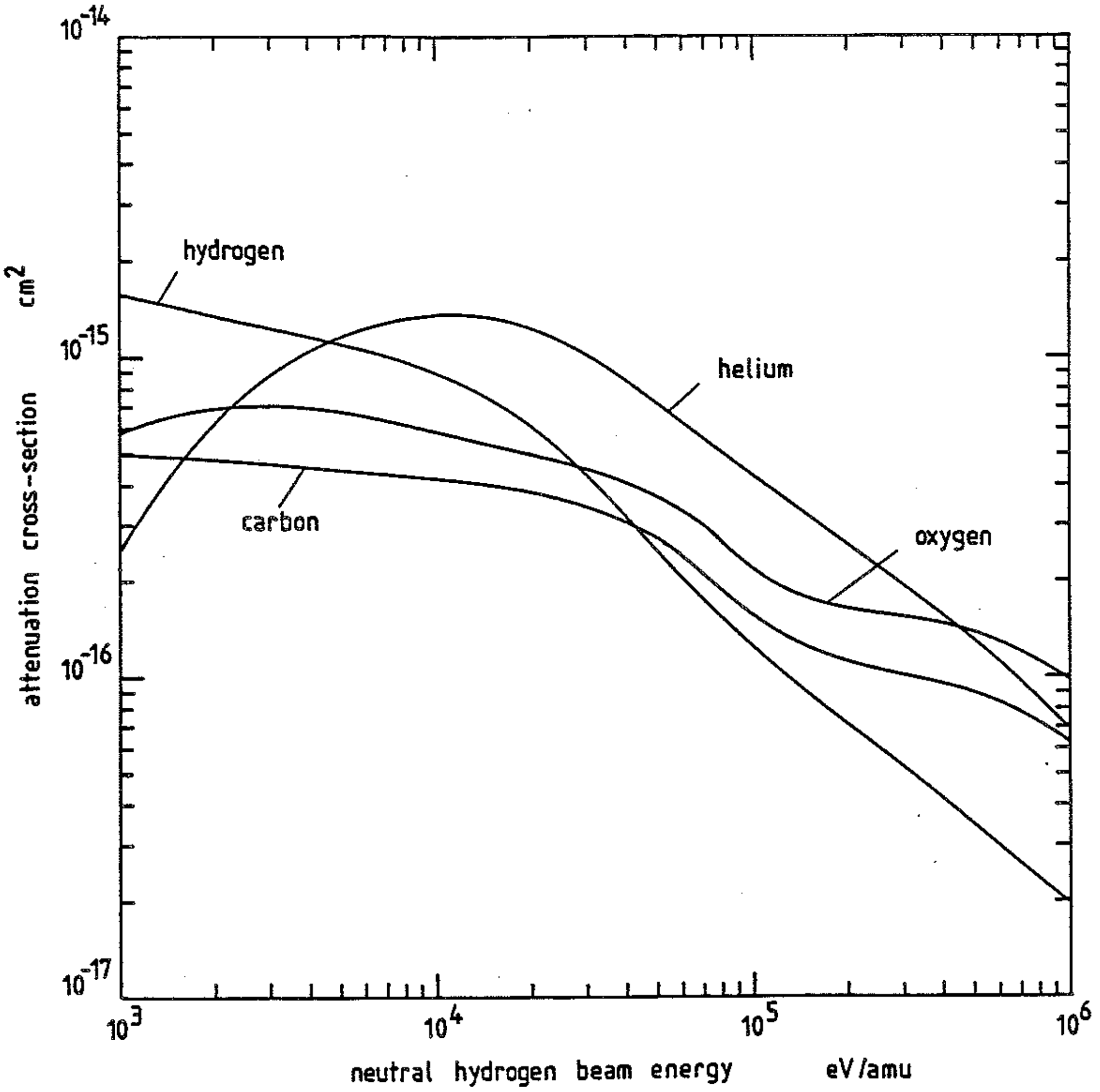

Fig.21 Cross-sections for neutral hydrogen beam attenuation by hydrogen and impurities.

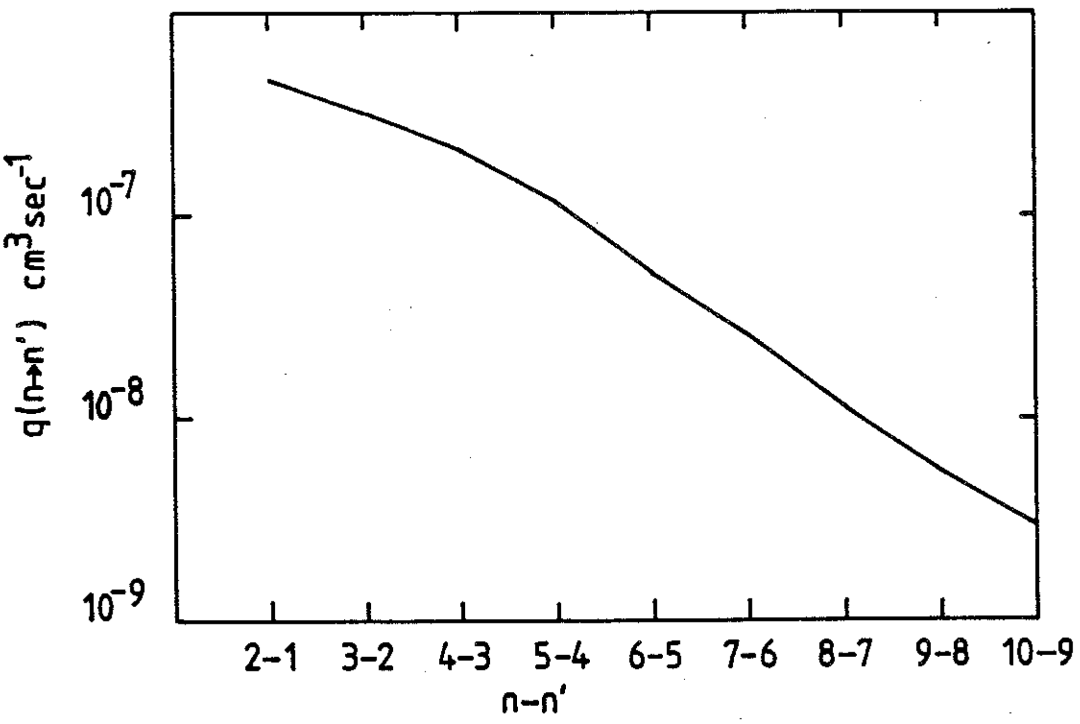

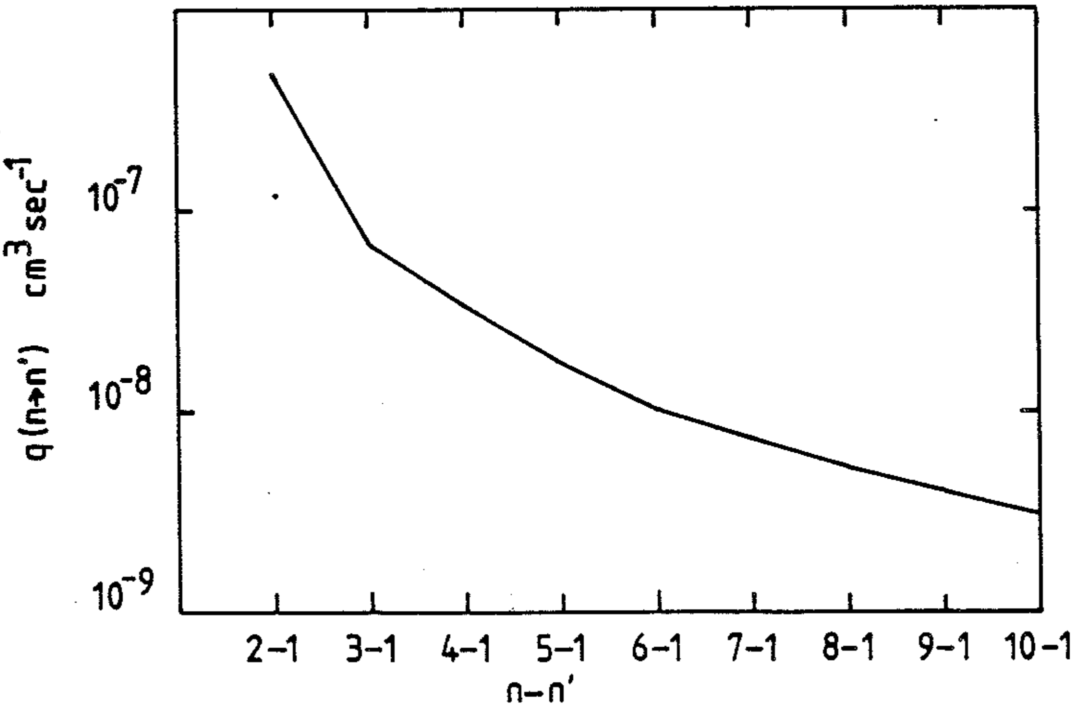

Fig.22 Series variation of effective charge exchange emission coefficients (CEM) following capture by C^{+6} from hydrogen beams in the 1s ground state (nℓj-picture). T_e=3.23keV, N_e=1.8x10^{13} cm^{-3}, T_i=2.16keV, N_i=1.3x10^{13} cm^{-3}, Z_{eff}=2. It is assumed that the hydrogen beam is monoenergetic of energy 5.0x10^{4}eV/amu.

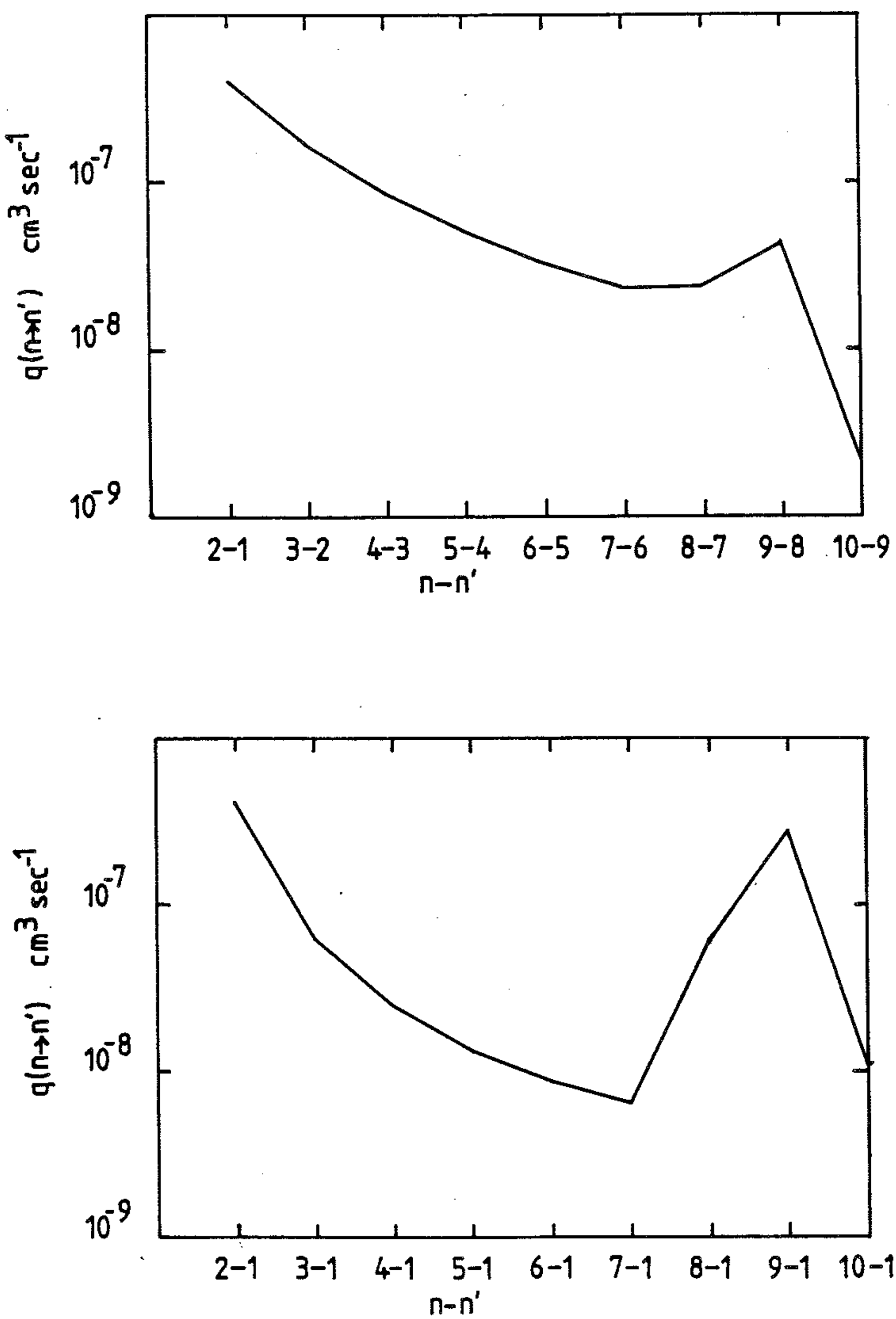

Fig.23 Series variation of effective charge exchange emission coefficients (CEM) following capture by C^{+6} from thermal hydrogen in the n=2 level (nℓj-picture). T_e=557eV, N_e=3.3x10^{12} cm^{-3}, T_i=143eV, N_i=2.3x10^{12} cm^{-3}, Z_{eff}=2. It is assumed that the hydrogen atoms all have the energy 143eV.

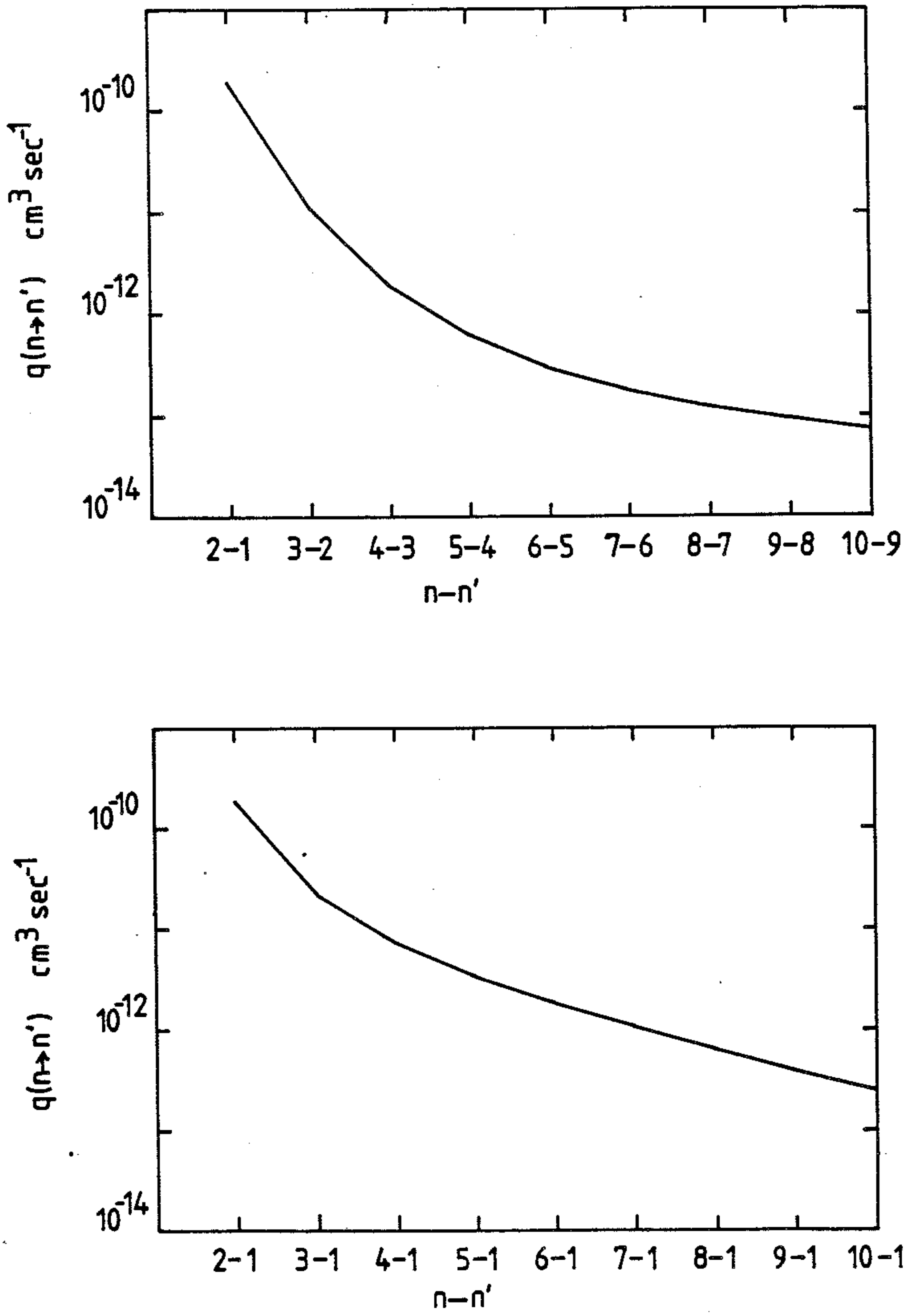

Fig.24 Series variation of effective excitation rate coefficients (EEM) (nℓj-picture) following excitation from the ground level of C^{+5}. T_e=900eV, N_e=6.9x10^{12} cm^{-3}, T_i=271eV, N_i=4.9x10^{12} cm^{-3}, Z_{eff}=2.

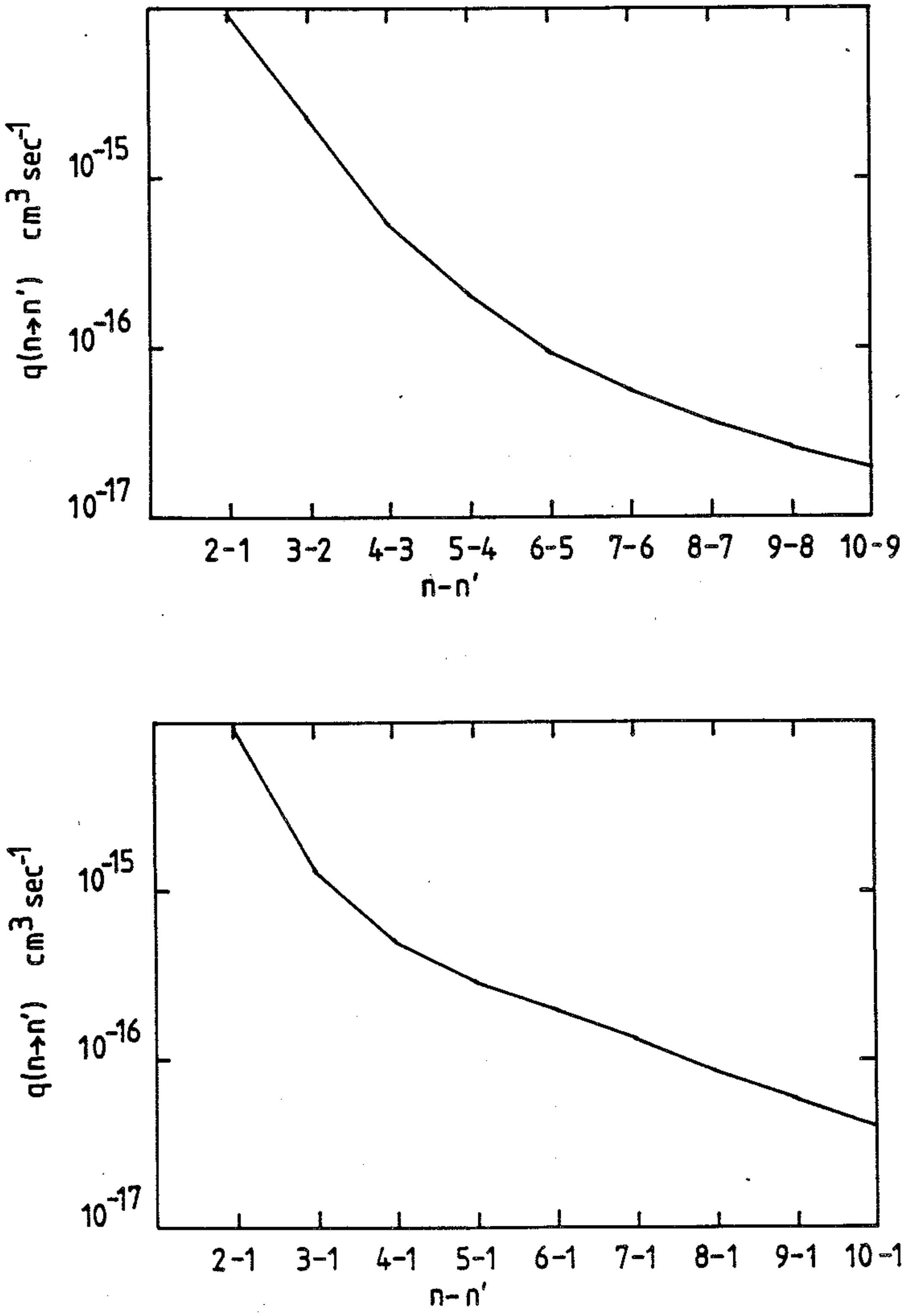

Fig.25 Series variation of effective radiative recombination rate coefficients (REM) (nℓj-picture) following capture by C^{+6}. T_e=3.23keV, N_e=1.8x10^{13} cm^{-3}, T_i=2.16keV, N_i=1.3x10^{13} cm^{-3}, Z_{eff}=2.

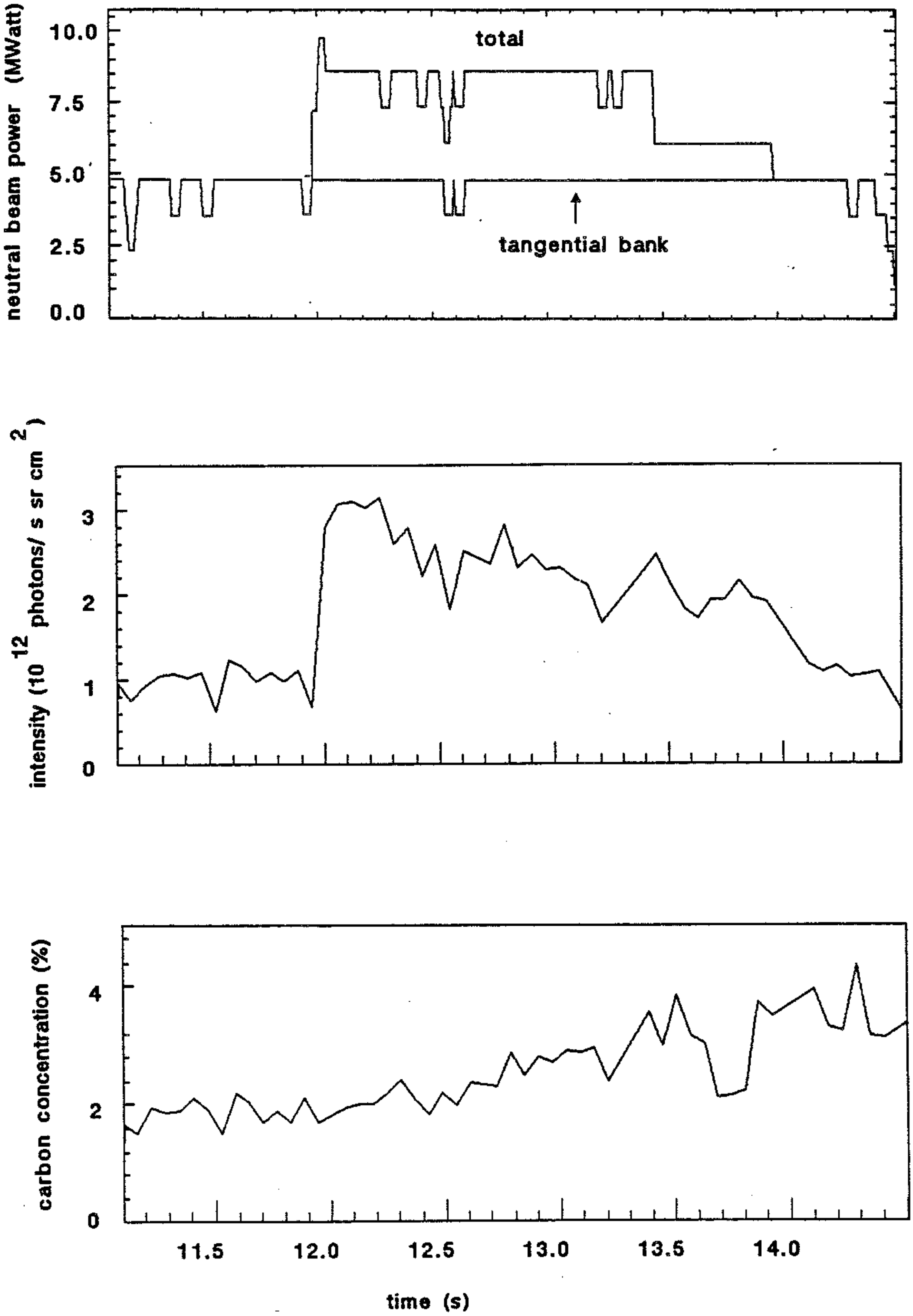

Fig.26 Evolution of the column emissivity and the carbon concentration for the carbon 5290.5 Å transition when the ratio of normal to tangential beams fired changes. (JET pulse 10762)

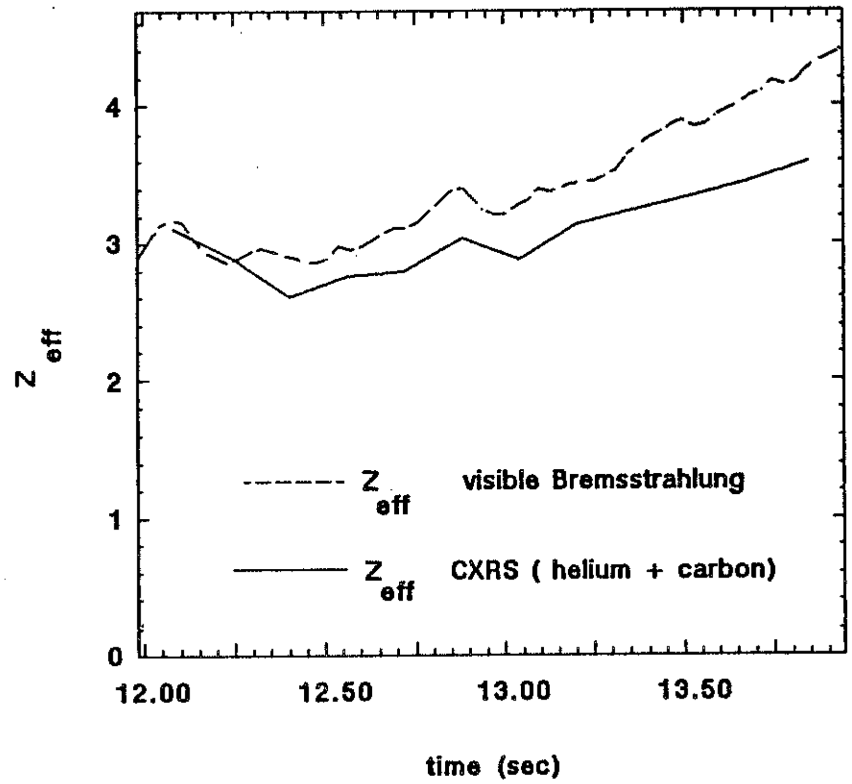

Fig.28 Comparison of Z_{eff} given by visible bremsstrahlung (dotted line) and CXRS measurements of helium (4686.3 Å) and carbon (5290.5 Å) during a helium discharge (JET pulse 10205). 2 MW of RF power is applied after 12.0 sec.

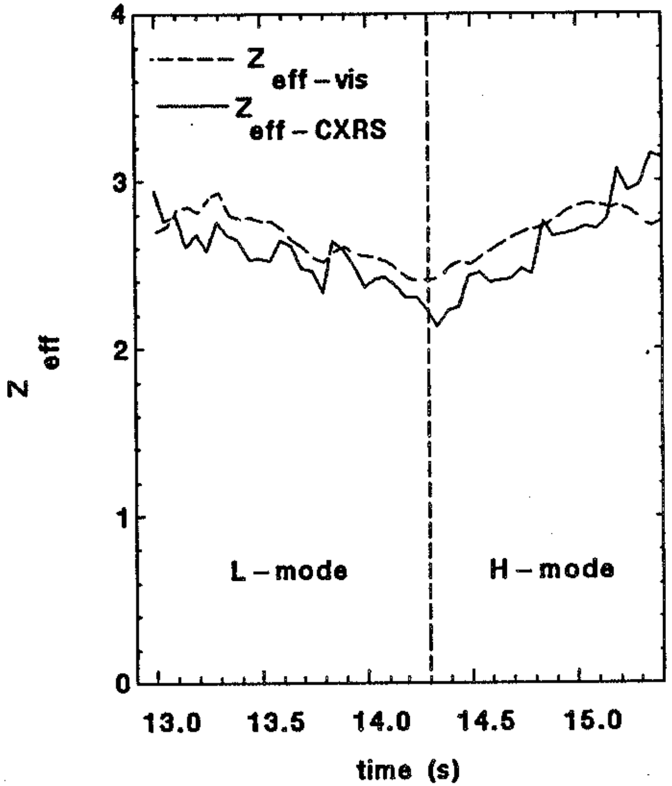

Fig.27 Z_{eff} deduced from CXRS using simultaneous measurement of carbon (5290.5 Å) and oxygen (4340.5 Å) densities is compared to the value obtained from visible bremsstrahlung (dotted line) during an X-point discharge (JET pulse 10793). Transition to the H-mode occurs at 14.0 sec.

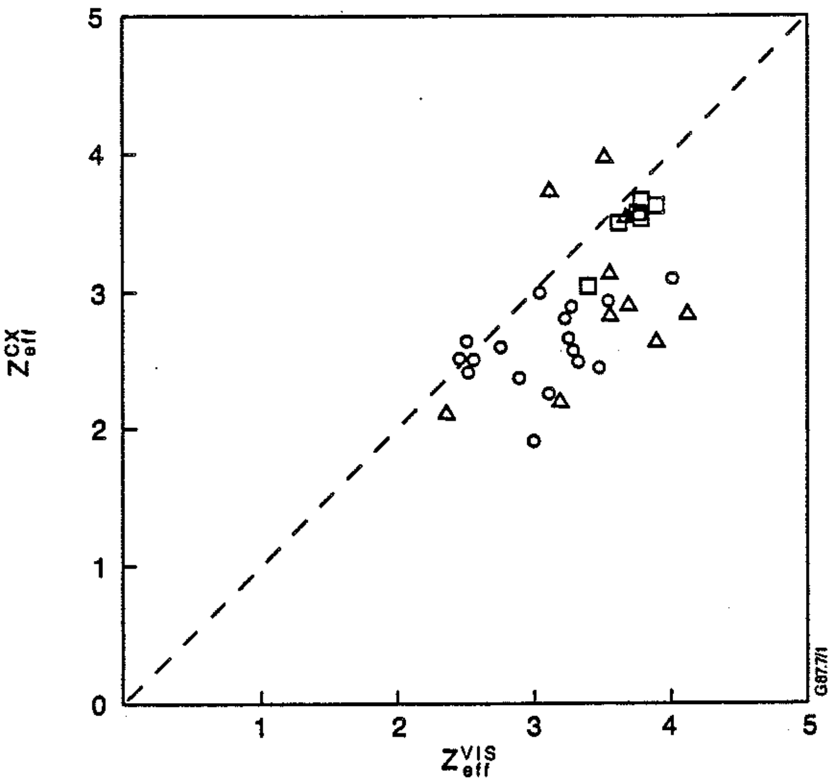

Fig.29 Comparison of Z_{eff} from visible bremsstrahlung and from CXRS for several JET pulses 1 sec after the beginning of neutral beam injection.

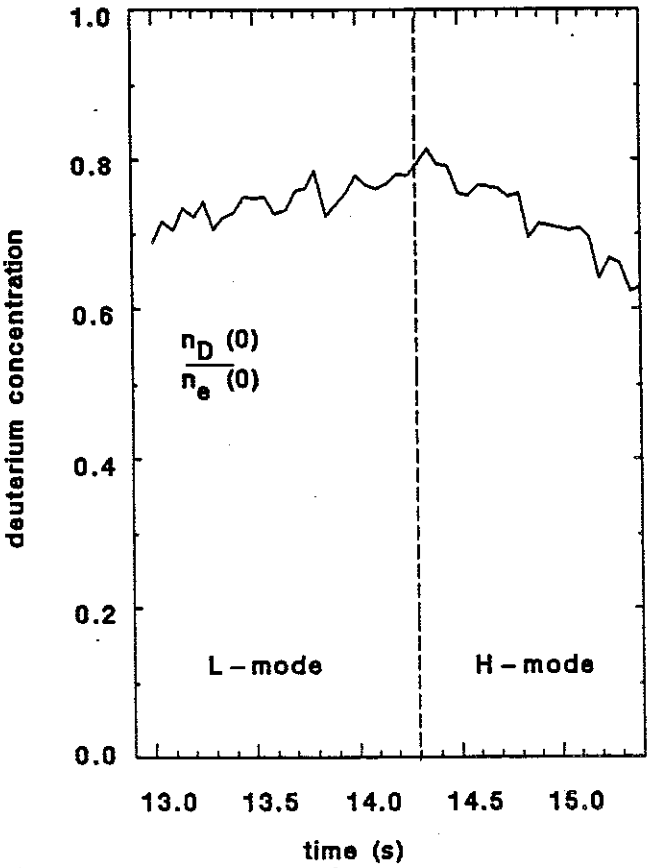

Fig.30 Evolution of the deuterium concentration during H-mode obtained by subtracting the carbon and oxygen contributions from the electron density on axis (JET pulse 10793).

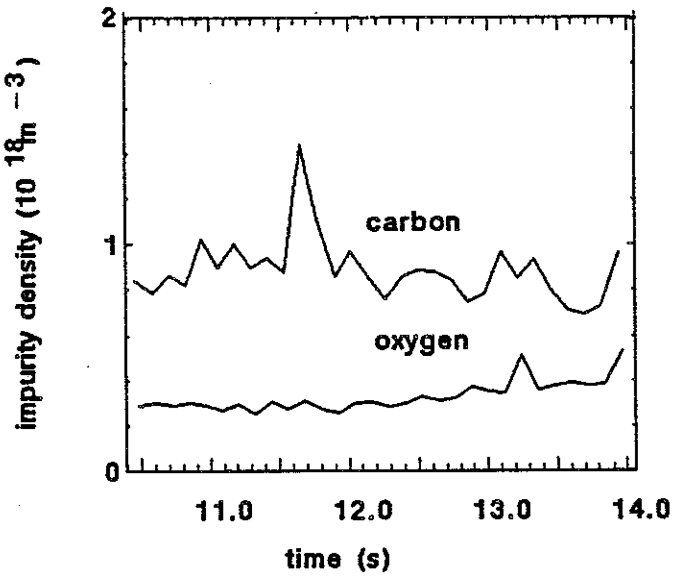

Fig.31 Carbon and oxygen densities for an inner wall discharge (JET pulse 10711).

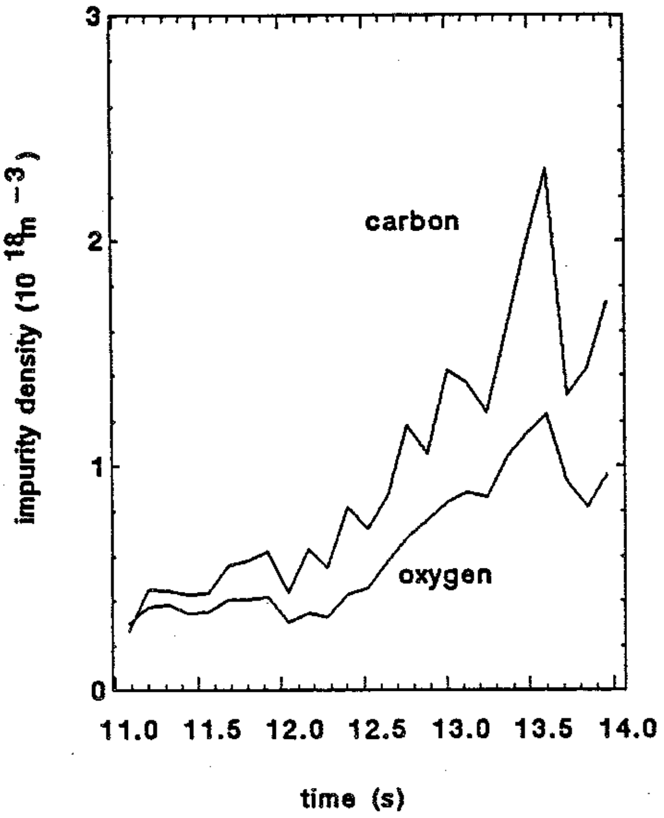

Fig.32 Carbon and oxygen density for a single null X-point discharge (JET pulse 10713).

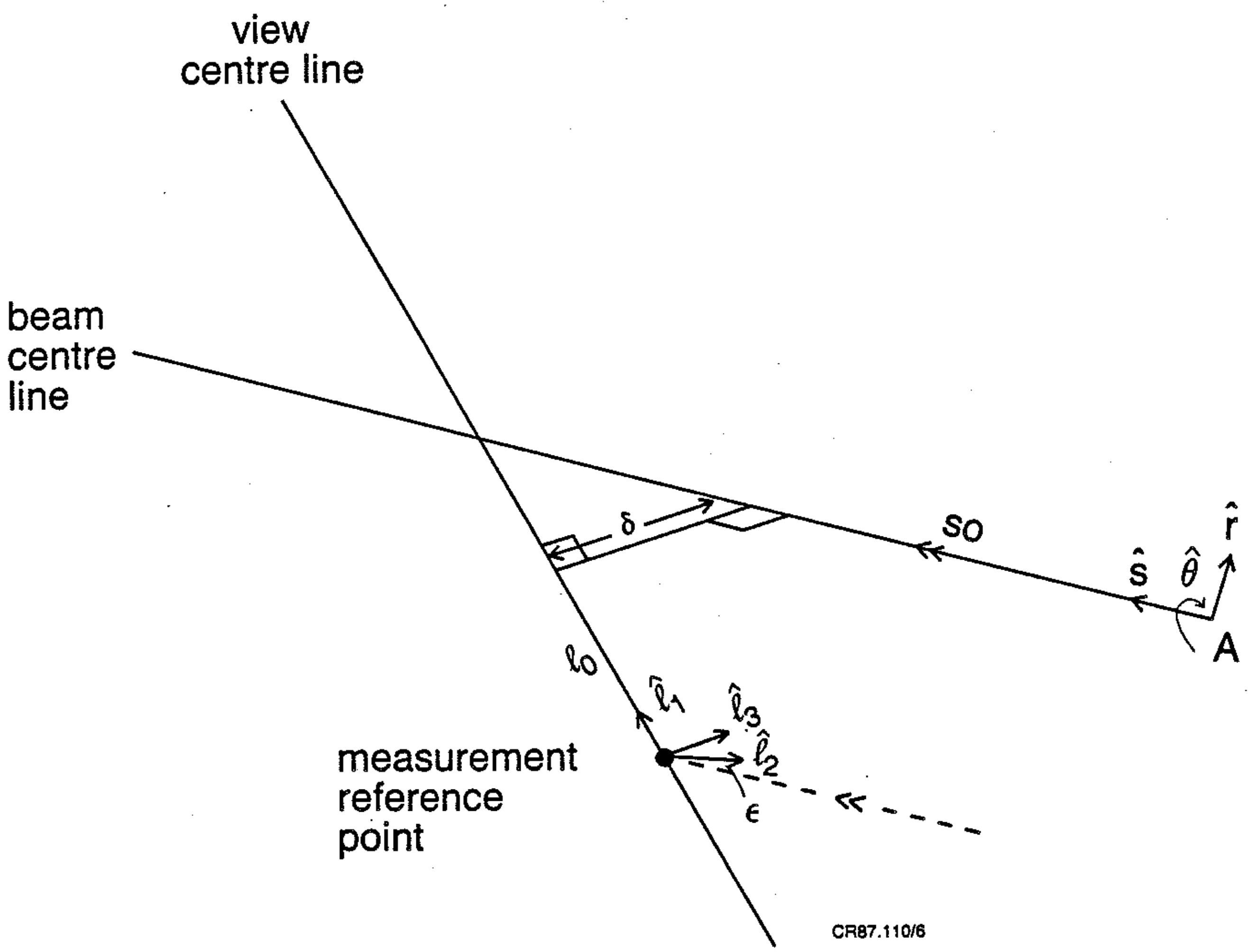

Fig.33 Coordinate system for neutral beam attenuation calculation.